batteries

MDPI

Article

What Differentiates Dielectric Oxides and Solid Electrolytes on the Pathway toward More Efficient Energy Storage?

Antonio Nuno Guerreiro [1], Beatriz Arouca Maia [1,2], Hesham Khalifa [1,3], Manuela Carvalho Baptista [1] and Maria Helena Braga [1,2,*]

[1] Engineering Physics Department, Engineering Faculty, University of Porto, 4200-465 Porto, Portugal
[2] LAETA—INEGI, Institute of Science and Innovation in Mechanical and Industrial Engineering, 4200-465 Porto, Portugal
[3] Department of Physics, Faculty of Science, Damanhur University, Damanhur 22511, Egypt
* Correspondence: mbraga@fe.up.pt

Abstract: Taking advantage of electrode thicknesses well beyond conventional dimensions allowed us to follow the surface plasmonic THz frequency phenomenon with vacuum wavelengths of 100 μm to 1 mm, only to scrutinize them within millimeters-thicknesses insulators. Here, we analyze an Al/insulator/Cu cell in which the metal electrodes-collectors were separated by a gap that was alternatively filled by SiO_2, MgO, Li_2O, $Na_3Zr_2Si_2PO_{12}$–NASICON, $Li_{1.5}Al_{0.5}Ge_{1.5}(PO_4)_3$–LAGP, and $Li_{2.99}Ba_{0.005}ClO$–Li^+ glass. A comparison was drawn using experimental surface chemical potentials, cyclic voltammetry (I-V plots), impedance spectroscopy, and theoretical approaches such as structure optimization, simulation of the electronic band structures, and *work functions*. The analysis reveals an unexpected common emergency from the cell's materials to align their surface chemical potential, even *in operando* when set to discharge under an external resistor of 1842 $\Omega.cm_{insulator}$. A very high capability of the metal electrodes to vary their surface chemical potentials and specific behavior among dielectric oxides and solid electrolytes was identified. Whereas LAGP and Li_2O behaved as p-type semiconductors below 40 °C at OCV and while set to discharge with a resistor in agreement with the Li^+ diffusion direction, NASICON behaved as a quasi n-type semiconductor at OCV, as MgO, and as a quasi p-type semiconductor while set to discharge. The capacity to behave as a p-type semiconductor may be related to the ionic conductivity of the mobile ion. The ferroelectric behavior of $Li_{2.99}Ba_{0.005}ClO$ has shown surface plasmon polariton (SPP) waves in the form of surface propagating solitons, as in complex phenomena, as well as electrodes' surface chemical potentials inversion capabilities (i.e., χ (Al) − χ (Cu) > 0 to χ (Al) − χ (Cu) < 0 vs. E_{vacuum} = 0 eV) and self-charge ($\Delta V_{cell} \geq +0.04$ V under a 1842 $\Omega.cm_{insulator}$ resistor). The multivalent 5.5 mm thick layer cell filled with $Li_{2.99}Ba_{0.005}ClO$ was the only one to display a potential bulk difference of 1.1 V. The lessons learned in this work may pave the way to understanding and designing more efficient energy harvesting and storage devices.

Keywords: dielectrics; semiconductors; solid electrolytes; ferroelectrics; scanning Kelvin probe; plasmons; self-charge

Citation: Guerreiro, A.N.; Maia, B.A.; Khalifa, H.; Baptista, M.C.; Braga, M.H. What Differentiates Dielectric Oxides and Solid Electrolytes on the Pathway toward More Efficient Energy Storage? *Batteries* **2022**, *8*, 232. https://doi.org/10.3390/batteries8110232

Academic Editor: Claudio Gerbaldi

Received: 3 October 2022
Accepted: 4 November 2022
Published: 10 November 2022

1. Introduction

As global energy utilization is anticipated to be doubled by the mid-century due to population and economic development, energy supplies are becoming more and more critical [1]. Hence, harvesting and storing renewable energy, such as solar energy, will be one of the most significant global development challenges over the incoming years [2].

Li-ion batteries have been pioneers and protagonists in electrification as they can store when harvested energy is abundant and deliver when it is scarce [3,4].

The significant advantages of Li-ion batteries are their energy/power densities; they may also complement fuel cells for higher energy density or capacitors for a higher power.

Capacitors can also charge batteries and recover energy harvested in vehicles, flying wheels, tribological devices, tides, and waves [5].

Li-ion batteries, however, raise safety problems [6]; they use materials that are not inexpensive and widely available such as cobalt [7], do not have an enlarged temperature range of utilization [8], and reach their theoretical capacity limit.

Alternatively, the implementation of materials with extraordinary capabilities in out-of-the-box devices that can address harvesting and storage tandemly (Figure 1), such as ferroelectrics [9], van der Waals quantum materials [10], axion insulators [11], and topologic photonic metamaterials [12], in well-established architectures, opens horizons toward a new revolution where devices have more than one role and are advanced on lessons learned from the shared behaviors.

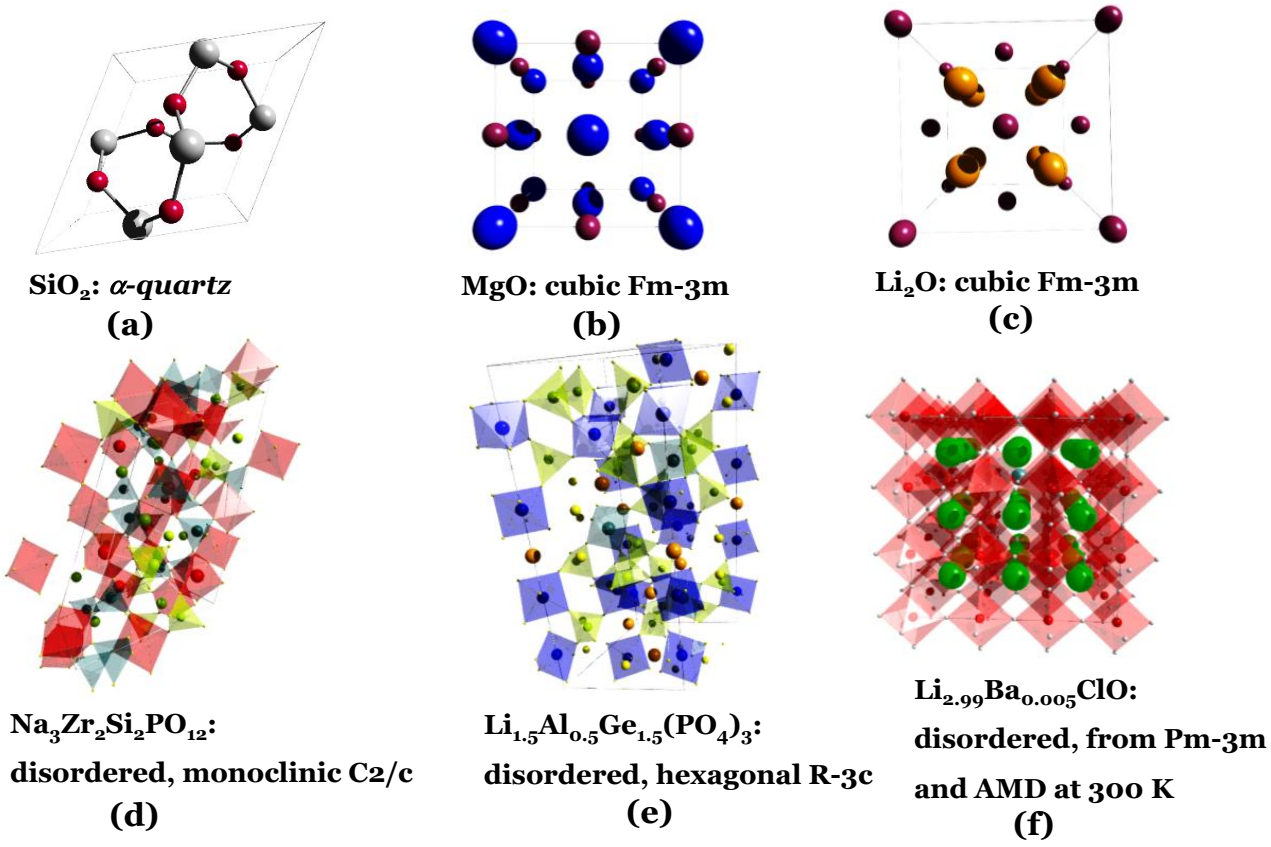

Figure 1. Crystal structures for the studied insulators. *Dielectric oxides*: (**a**) SiO_2 trapezohedral, P3221 (sg# 154); red spheres: O; (**b**) MgO cubic, Fm-3m, (sg# 225); wine-red spheres: O; (**c**) Li_2O cubic, Fm-3m, (sg# 225); wine-red spheres: O; *dielectric solid electrolyte*: (**d**) room temperature $Na_3Zr_2Si_2PO_{12}$–NASICON, monoclinic, C2/c (sg#15); octahedral: ZrO_6; tetrahedral: PO_4/SiO_4 sharing common corners; (**e**) $Li_{1.5}Al_{0.5}Ge_{1.5}(PO_4)_3$–LAGP, rhombohedral, R-3c (sg#167); octahedral: AlO_6/GeO_6; tetrahedral: PO_4; orange spheres: Li; yellow spheres: O. (**f**) $Li_{2.99}Ba_{0.005}ClO$–Li^+-glass optimized structure using ab initio molecular dynamics at 300 K from the initial cubic structure Pm-3m (sg# 221). octahedral: OLi_6; green-blue (small) sphere: Ba; green spheres: Cl. ***Note:*** the dielectrics were chosen due to their applications and relative *work functions*: WF(SiO_2) > WF(Cu) > WF(Al), WF(Cu) > WF(Al) > WF(MgO), and WF(Cu) > WF(Li_2O) > WF(Al).

The advent of solid-state batteries demands knowledge of the interplay phenomena between electrodes, interphases, interfaces, and the solid electrolyte at different pressures, temperatures, and cycle numbers [13–15]. The entangled behavior is even more critical *in operando* (Figure 2a). The conjunction of experimental techniques with theoretical simulation is therefore paramount, especially for understanding the driving forces within the battery cell that mostly result from the differences in chemical potentials (analyzed with impedance

spectroscopy EIS and cyclic voltammetry CV) and surface chemical potentials (analyzed with scanning Kelvin probe SKP) within the cell. The flow of charges is dependent on the bulk and surface potentials, as shown herein.

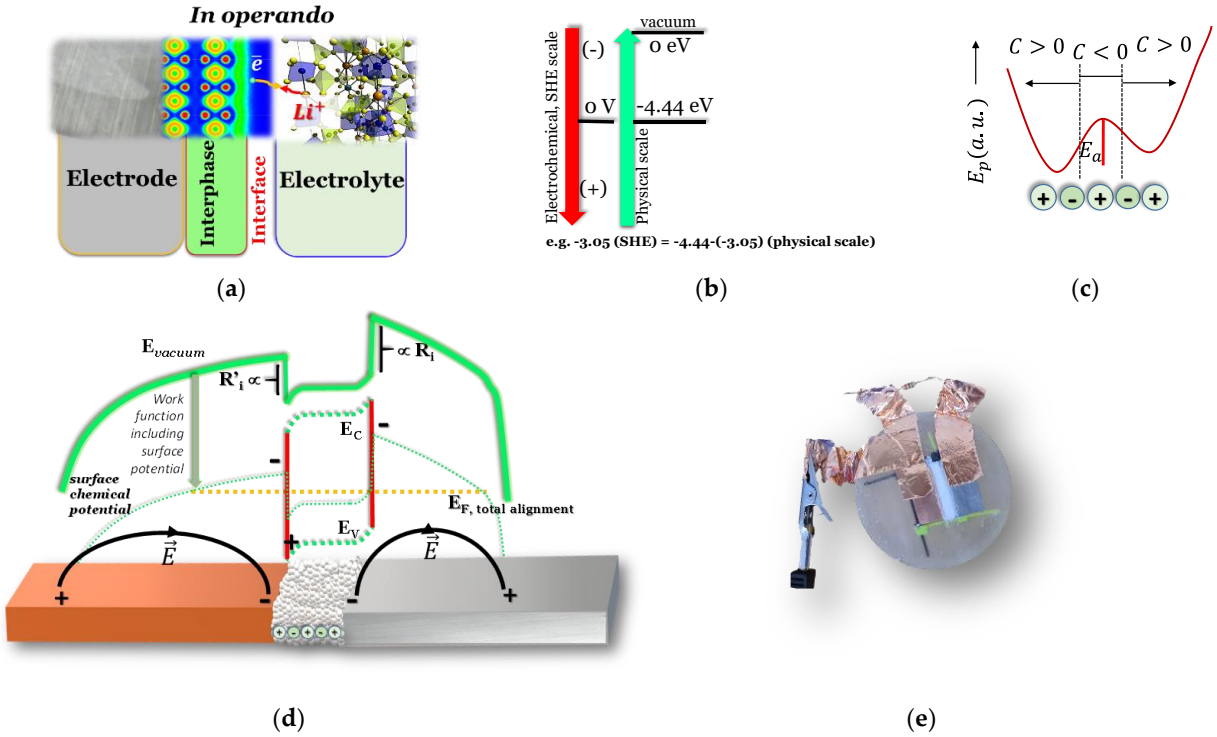

Figure 2. (**a**) Schematic interplay of the constituents of a battery cell *in operando*; (**b**) absolute chemical potentials having as reference the standard hydrogen electrode (SHE) and the vacuum at 0 eV in the physical scale that relates more directly with the work functions of the materials; (**c**) potential energy E_p showing positive polarization at both interfaces of a cell containing a dielectric. The maximum corresponding to the activation energy, E_a, is a metastable configuration where both ends have equal polarization signs; (**d**) extended electrode highly resistive cells, where the contact is made difficult by quantum wells/barriers, and each electrode aligns the surface chemical potentials with the dielectric, independently; but, along the cell, there is at least one point for which all the chemical potentials equalize. The latter energy may correspond to the Fermi level or electrochemical potential. The internal contact happens through the electric field, made possible by SPP; (**e**) photo of a Zn/SiO_2/Cu cell used to perform the SKP analysis when connected to a resistor. ***Note:*** the Al/insulator/Cu used had Al and Cu tapes connected to the resistor and SKP instrument to avoid additional heterojunctions.

A few questions then stand up: *what differentiates the materials that possess specific electrical properties while working in the same solid-state device? What is the most efficient solid electrolyte relative to its chemical potential? How can the propagation of the electric field throughout the cell due to plasmon polariton affect the behavior of all-solid-state batteries?*

Dielectric materials are electrical insulators that become polarized when submitted to an electric field and have applications in almost all electronic devices, such as heterojunctions, transistors, memories, photovoltaics, capacitors, and batteries [16–18]. Dielectrics include all the other classes of materials that were studied in detail: **(1)** n- and **(2)** p-type intrinsic semiconductors, **(3)** solid electrolytes, and **(4)** ferroelectric solid electrolytes.

Here, the study of SiO_2, MgO, and Li_2O dielectric oxides, $Na_3Zr_2Si_2PO_{12}$, $Li_{1.5}Al_{0.5}Ge_{1.5}(PO_4)_3$ and $Li_{2.99}Ba_{0.005}ClO$ solid electrolytes, and a detailed examination of the surface chemical potentials in an Al/insulator/Cu cell was carried out at OCV and *in operando*. Ab initio simulations were also performed to understand the surface electrical properties of the dielectrics and their role in the cell. The crystal structure of the materials is well known to influence their electronic and electrochemical performance, and so are the properties described in Table 1. In Figure 1, these materials' crystal

structures and space groups are also shown. In the Supplementary Information (SI), the detailed properties of these materials that help identify similarities and differences in their performances in all-solid-state devices, and their actual applications, are discussed.

Table 1. Physical properties of the studied dielectrics and solid electrolytes.

Material	Type	Dielectric Constant at RT and 0.1 Hz (ε_r)	Ionic Conductivity at RT ($S \cdot cm^{-1}$)	Refs.
SiO_2	Dielectric	3.9	-	[19]
MgO	Dielectric	10	10^{-36}	[20,21]
Li_2O	Dielectric	8–11	10^{-12}	[22]
$Na_3Zr_2Si_2PO_{12}$ (NASICON)	Solid Electrolyte	10^3–10^4	10^{-4}	[23,24]
$Li_{1.5}Al_{0.5}Ge_{1.5}(PO_4)_3$ (LAGP)	Solid Electrolyte	-	10^{-4}–10^{-3}	[25]
$Li_{2.99}Ba_{0.005}ClO$ (Li^+ glass)	Ferroelectric Solid-electrolyte	10^7–10^9	10^{-2}	[26,27]

2. Materials

2.1. Oxides

The oxides in this study used as dielectrics were powders of (1) Silicone oxide (IV) 99.5%, powders' diameter <44 µm from Thermo Fisher; (2) Magnesium oxide (MgO) 99.95%, powders' diameter <44 µm from Alfa Aesar; and (3) Lithium oxide (Li_2O) 99.5 %, powders' diameter <149 µm, from Alfa Aesar. All oxides were kept and manipulated to fill the cell's gap in a glovebox with an argon atmosphere.

2.2. Solid Electrolytes

The solid electrolytes used were powders of (1) $Na_3Zr_2Si_2PO_{12}$ with diameters < 44 µm from MSE supplies; (2) $Li_{1.5}Al_{0.5}Ge_{1.5}(PO_4)_3$, with diameters varying from 0.30 to 0.50 µm from Ampcera; and (3) $Li_{2.99}Ba_{0.005}ClO$ was prepared in the laboratory environment, synthesized by water solvation, similarly as presented by Braga et al. [16,28]. After obtaining a solid-state material, the electrolyte was closed hermetically and dried at 250 °C. After the drying process finished, the Li^+-glass was kept in a glovebox with an argon atmosphere and grounded with an Agate ball milling equipment in a hermetic sample holder for 40 min (300 rpm) using a ball milling machine with an Agate container and five balls with a diameter of 20 mm. All solid electrolytes were manipulated inside the Ar-filled glovebox (O_2 and H_2O < 1 ppm) while filling the cell's gap.

2.3. Cells

The cells were fabricated with two different metal electrode pairs (aluminium//copper) or (zinc//copper) with a designed parallelepiped gap between them that was filled with oxides or solid electrolytes. The electrodes were fixed on the epoxy support. The average dimensions of the Al/insulator powder sample/Cu cell's materials used in the experiments were Al with (11 × 20 × 4.7) mm^3; powder sample oxide or solid electrolyte with (5.5 × 22 × 4.7) mm^3; and Cu with (11 × 20 × 4.7) mm^3 (Figure 2).

3. Methods

3.1. Cell Preparation

Before beginning the calibration procedures on SKP, it was necessary to prepare the cell according to the following process: (1) sand and polish the electrodes; (2) thoroughly clean the particles' residues; and (3) fully dry the cell. Afterward, the cell's gap between the electrodes was ready to be filled with oxide or electrolyte powder, tightly compressed with a spatula-like tool, and leveled by the electrodes. The oxide or the electrolyte was also thoroughly dried before this latter procedure.

3.2. Scanning Kelvin Probe (SKP)

SKP is a non-invasive and non-contact technique based on the contact potential difference (CPD) between two electrically connected metals [29]. A vibrating capacitor tip measures the local work function difference between the sample and the tip, which is related to the surface chemical potential [30] (Figure 2d). Therefore, the SKP technique allows an electrochemical study of the materials' surface. SKP technique was also used to map the topography of the surface's materials performing the Capacitive Tracking Measurement (CTM). This technique is appropriate for non-flat surfaces and irregularities; it maintains a constant distance between the probe tip and the sample, scanning the surface without losing information about the cell's surface. These techniques are under the atomic force microscopy (AFM) set of methods. All SKP measurements were performed with a Biologic SKP-M470 with an SKP tip U-SKP-370/1 made of tungsten wire with 500 µm diameter and an SKP tip U-SKP-150, made of tungsten wire with 150 µm diameter. The distance between the CTM or SKP probe tip and the sample was 100 µm (oxides and solid electrolytes) to 200 µm (ferroelectric solid electrolyte), and the analysis was monitored through a micro camera. All experiments were performed in a dry box. It is worth highlighting that each set of experiments, for each insulator, was served with fresh materials after cleaning and drying the cell. We give knowledge of the most representative experiments that illustrate the materials' behaviors.

The chemical potential μ is equal to the surface chemical potential $\chi = E_{vacuum} - WF = \mu + z_i F\phi$, when the surface potential ϕ is null, where $E_{vacuum} = 0\,eV$, WF is the *work function*, z_i is the valency of the interfacial ion, and F the Faraday constant (more detail in [31]). Therefore, the experimental WF of each material, herein, was obtained for the inner surface away from the interfaces.

Upon equalization due to electrical contact between two materials, the electrochemical potentials $\overline{\mu}$, or Fermi levels E_F, $\Delta\overline{\mu} = 0 = \Delta\mu - z_i F\Delta V$, and the chemical potentials should correspond to $\Delta\mu = z_i F\Delta V$ via the formation of double layer capacitors (EDLC) with a potential difference, $\Delta V = \Delta\phi$ where $\Delta\phi$ is the difference of surface potentials of the interfacial materials. Consequently, E_F is obtained where there is an equalization of χ at the interfaces of the dielectric or solid electrolyte with the electrodes. When the equalization is not possible at the two interfaces electrode$_1$/insulator/electrode$_2$ due to a potential well translated in an interfacial resistance, the equalization point for one of the electrodes is obtained away from the interface. The equalization of χ is achieved through the surface plasmons or electric field propagation across the electrodes.

3.3. Electrochemical Impedance Spectroscopy (EIS) and Cyclic Voltammetry (CV)

In EIS, a GAMRY (GAMRY1000) impedance meter imposes a small amplitude AC signal to the cell's terminals. The AC voltage and current response of the sample cell allow for determining the impedance (resistive, capacitive, and inductive characteristics) of the cells and equivalent circuits related to their components at controlled frequencies. The EIS studies complemented the study of the surface phenomenon in the cells. EIS was performed in the frequency range of 1 MHz to 0.1 Hz with an amplitude signal of 10 mV.

Cyclic Voltammetry (CV) is an electrochemical technique used for providing information about the dynamic behavior of the cells while performing cycles under an imposed voltage rate. CV measurements with the present cells were performed within the potential window of −0.35 V to +1.0 V and scan rates of 25 mV·s^{-1} and 2 mV·s^{-1}.

3.4. Ab Initio Simulations

The study of the material's surface properties is critical. Ab initio simulations were accomplished using Density Functional Theory (DFT) and the Generalized Gradient Approximation (GGA) pseudopotential method to determine the lattice constant, lattice stability, band structure, surfaces, and *work functions* at different temperatures. These simulations used crystal representations without introducing defects such as vacancies, and impurities, as our previous work on ZnO did [31].

DFT and hybrid functional HSE06 packages, as implemented by VASP6 (Vienna Ab initio Simulation Package) [32], were performed with a plane-wave cutoff of >400 eV, reciprocal space projection, and spacing of k points of 0.3 $Å^{-1}$. Electron localization functions (ELF) were obtained for each oxide (001) surface.

Ab initio molecular dynamics (AMD) was employed to simulate a closed system thermostatted in a heat bath at a constant temperature and pressure NP'T. The system was the crystalline $Li_{79}BaCl_{27}O_{27}$ optimized structure (from Pm-3m) after performing microcanonical simulation NV'E to set the temperature of 300 K (27 °C).

Macroscopic average potentials were calculated for 10 Å, and *work functions* were determined by calculating the difference between the maximum potential where electrons are at rest on the surface and the average potential between the minimum and maximum potentials (immediately before and after the line that marks the surface), corresponding to the Fermi level.

4. Results and Discussion

The AFM and SKP analyses in this study have shown *emergent phenomena.* The work functions or surface chemical potentials align in spite of any texture or mechanical stress introduced by the preparation of the surfaces or asymmetric oxidation. The cell rules the equalization of the surface potentials, even at an open circuit voltage (OCV), whereas one of the electrodes connects the cell through the insulator powder that disjoints both electrodes and fills the gap. Herein, we have used both the SHE and the Physical scales in Figure 2b to compare the surface chemical potentials. Figure 2c shows the potential energy E_p versus the polarization of the dielectric or ferroelectric; the most energetic configuration corresponds to both ends or opposite surfaces polarized with the same sign. The capacitance *C* is also shown for the different regions. This configuration for the potential energy is approximated to a quantum square barrier. As demonstrated herein, the dielectric with higher work functions than both the metallic electrodes will polarize, as shown in Figure 2c. With Fermi levels equalizing at interfaces $metal_1$/dielectric/$metal_2$, the dielectric material charges positively to compensate for the higher chemical potentials of the metal electrodes. A more negatively charged maximum in the inner surface of the dielectric balances the same sign polarizations at the interfaces with the metals. Nonetheless, if not enough time is given for the cell to relax with the dielectric, the polarization is straight and more negative on the interface with the Al or Zn (negative electrode), as commonly represented in the literature [33].

When the cell's surface is scanned along 1.2 cm (Table 2), the equalization of the three surface chemical potentials is not always clear, but the tendency is observed. When the cell is scanned for >2.0 cm, the alignment is almost always demonstrated (schematics of Figure 2d and Table 2), especially when the cell is at OCV. Depending on the dielectric's work function and resistance at the interfaces, the equalization of the surface potentials is obtained in different ways. The aluminum bends sharply for dielectrics ZnO [31], Li_2O, $Na_3Zr_2Si_2PO_{12}$, or $Li_{1.5}Al_{0.5}Ge_{1.5}(PO_4)_3$ or curves from the interface, with the surface chemical potentials passing through the point where the alignment between the three materials, electrodes, and dielectric is obtained. It is likely that the distance between the interface and the point at which the electrodes assume the same surface chemical potential as that of the interface is dependent on the quantum barrier/well or internal resistance at the interface (Figure 2d). The work function, including the surface potential, accounts for the surface chemical potential, which reflects the shape of the vacuum surface. For the insulators, the latter surface reflects the bending of conduction and valence bands (Figure 2d).

Table 2. Physical information is extracted from AFM, SKP, electrochemical analysis, and ab initio simulations for the cell when the insulator is a dielectric oxide or a solid electrolyte. ***Note***: calculated: μ_{Cu} = +0.14 V, SHE [31]; experimental: μ_{Cu} = +0.12 V, SHE; calculated: μ_{Al} = +0.25 [31] to +0.63 V, SHE; experimental: μ_{Al} = −1.01 V, SHE; calculated μ_{Zn} = −0.95 V, SHE [31]; experimental: μ_{Zn} = −0.42 V, SHE.

Cell Insulator: d = 5.5 mm S = 22 × 4.7 mm^2	**Circuit** Open OCV or close with an external resistance R	**Heterojunction equilibrium** and correspondent surface chemical potential (it may include parts of the electrode away from the surface that equalize as well)	**Heterojunctions surface chemical potential** difference (V)	**Maximum surface potential difference for the electrodes** at the interface with the insulator (V)	**- Bulk potential** difference for the cell **- Temperature - Dew point, DP**
Dielectric: **SiO_2** [$\Delta V_{SiO_2(Cu)} - \Delta V_{SiO_2(Al)}$ = 0.60-(0.77) = 0.17 V Figure 3a; $\Delta V_{SiO_2(Al)} - \Delta V_{SiO_2(Cu)}$ = 0.44–0.59 = −0.15 V] Figure 3b					
Calculated surface chemical potential (*ab initio*), μ = +0.99 V, SHE; experimental: μ = +0.73 V, SHE					
Cu/SiO_2/Al	OCV	Cu1 … Cu2/SiO_2 0.22 V	0.36	0.65	–
Al/SiO_2/Cu	OCV	Al1 … Al2/SiO_2 −0.15 V	0.36	0.73	–
Al/SiO_2/Cu	OCV	SiO_2/Cu1 … Cu2 0.21 V			
Cu/SiO_2/Al	OCV	Cu1 … Cu2/SiO_2 0.44 V	0.53	0.59	V_i: 12 mV V_f: 13 mV 38 °C DP: <10 °C
Cu/SiO_2/Al	OCV	Cu … SiO_2/Al 0.09 V			
Zn/SiO_2/Cu	OCV	Zn/SiO_2 … Cu1 … Cu2 −0.059 V	0.33	0.30	–
Zn/SiO_2/Cu	OCV	SiO_2/Cu 0.29 V			
Dielectric: **MgO** [$\Delta V_{MgO(Al)} - \Delta V_{MgO(Cu)}$ = −1.56-(−1.03) = −0.53 V; $\Delta V_{MgO(Cu)} - \Delta V_{MgO(Al)}$ = −0.27-(−0.61) = 0.34 V] Figure 4d					
Calculated surface chemical potential (*ab initio*), μ = −1.18 V, SHE; experimental: μ = −1.12 V, SHE					
Cu/MgO/Al	OCV	Cu1 … Cu2/MgO … Al 0.60 V	0.43	0.50	
Cu/MgO/Al	OCV	MgO/Al1 … Al2 0.17 V			
Al/MgO/Cu	OCV	Al1 … Al2/MgO −1.24 V	0.43	0.92	V_i: 9.5 mV 25 °C V_f: 15 mV 36 °C DP: <10 °C
Al/MgO/Cu	OCV	Al1 … MgO/Cu −0.81 V			
Cu/MgO/Al	OCV	Cu1 … Cu2/MgO … Al 0.01 V	0.36	0.46	
Cu/MgO/Al	OCV	MgO/Al −0.35 V			
Dielectric: **Li_2O** [$\Delta V_{Li_2O(Cu)} - \Delta V_{Li_2O(Al)} \approx 0$ V] Figure 5b,d					
Calculated surface chemical potential (*ab initio*), μ = +0.058 V, SHE; experimental: μ = +0.074 V, SHE					
Cu/Li_2O/Al	OCV	Cu/Li_2O … 0.13 V	0.26	0.37	V_i: 11 mV V_f: 10 mV 25 °C DP: <10 °C
Cu/Li_2O/Al	OCV	Li_2O/Al1 … Al2 −0.13 V			
Al/Li_2O/Cu	OCV	Al1 … Al2/Li_2O −0.36 V	0.23	0.42	–
Al/Li_2O/Cu	OCV	Li_2O/Cu −0.13 V			
Cu/Li_2O/Al	OCV	Cu1 … Cu2/Li_2O 0.12 V	0.14	0.38	–
Cu/Li_2O/Al	OCV	Li_2O/Al1 … Al2 −0.023 V			

Table 2. *Cont.*

Cell Insulator: d = 5.5 mm S = 22 × 4.7 mm^2	**Circuit** Open OCV or close with an external resistance R	**Heterojunction equilibrium** and correspondent surface chemical potential (it may include parts of the electrode away from the surface that equalize as well)	**Heterojunctions surface chemical potential** difference (V)	**Maximum surface potential difference for the electrodes** at the interface with the insulator (V)	- **Bulk potential** difference for the cell **- Temperature - Dew point, DP**
Solid electrolyte: **$Na_3Zr_2Si_2PO_{12}$–NASICON** [band bending as an n-type semiconductor, OCV] Figure 6a,b; solid electrolyte: [band bending as p-type semiconductor, R = 980 Ω] Figure 6c,d					
Calculated surface chemical potential (*ab initio*), μ = −0.67 V (001) and −0.37 V (010), SHE; experimental: μ = +0.26 V, SHE					
Cu/NASICON/Al	OCV	Cu1 … Cu2/NASICON/Al 0.21 V	~0	0.64	V_i: 34 mV V_f: 10 mV 34 °C DP: <10 °C
Cu/NASICON/Al	980 Ω	Cu1 … Cu2/NASICON/Al 0.004 V	~0	0.58	V_i: 29 mV V_f: 30 mV 36 °C DP: <10 °C
Solid electrolyte: **$Li_{1.5}Al_{0.5}Ge_{1.5}(PO_4)_3$–LAGP** [band bending as a p-type semiconductor, OCV and R = 980 Ω] Figure 7					
Calculated surface chemical potential (*ab initio*), μ = +0.81 V, SHE; experimental: μ = +0.52 V, SHE					
Cu/LAGP/Al	OCV	Cu1 … Cu2/LAGP/Al 0.25 V	~0	0.67	V_i: 13.47 mV 25 °C V_f: 92.03 mV 35 °C DP: <10 °C
Cu/LAGP/Al	980 Ω	Cu1 … Cu2/LAGP/Al 0.23 V	~0	0.67	V_i: 92.73 mV V_f: 0.100 V 36 °C DP: <10 °C
Solid electrolyte and ferroelectric: **$Li_{2.99}Ba_{0.005}ClO$–Li^+ glass**, Figure 8 (insulator thickness 5.5 mm)					
Calculated surface chemical potential (*ab initio*), μ = +0.25 V, SHE; experimental: μ = +0.23 V, SHE					
Cu/Li^+glass/Al	OCV	Cu1 … Cu2/Li^+glass1 … 2 0.21 V	+0.25	+0.29	V_i = 1.14 V V_f = 0.89 V 36 °C DP: <10 °C
Cu/Li^+glass/Al	OCV	Li^+glass/Al1 … Al2 −0.04 V			
Cu/Li^+glass/Al	OCV	Cu1 … Cu2/Li^+glass1 … 2 0.25 V	+0.13	+0.087	**V_i = 0.89 V V_f = 0.93 V** 36 °C DP: <10 °C
Cu/Li^+glass/Al	OCV	Li^+glass/Al1 … Al2 0.12 V			
Al/Li^+glass/Cu	980 Ω	Al/Li^+glass/Cu1 … Cu2 0.25 V	**−0.15**	**−0.68**	**V_i = 0.91 V V_f = 0.94 V** 36 °C DP: <10 °C

For other dielectrics such as MgO, which have demonstrated a slightly lower work function than electrically insulated aluminum, a sharp decrease in the surface chemical potential toward the equalization point happens at the Cu/MgO interface, mirroring the process for ZnO [31] at the ZnO/Al heterojunction. This result remits to the surface plasmons polaritons (SPP) and the electrostatic interactions throughout the surface of the cell characteristics of the insulator/metal interfaces [34]. Additionally, the present findings may be related to Rogue waves [35] observed in Al surface chemical potential when the insulator is MgO. The Rogue waves are solitons that allow for the equalization of the surface chemical potential at 0.60 V (Table 2), as shown hereafter.

Dielectrics. SiO_2 is a well-known dielectric used in the gate of field-effect transistors (FET) since the 1950s, after the discovery of the suppression of the Si's surface states by its presence. Silicon dioxide (Figure 1a, Table 1) is a very stable dielectric and is not hygroscopic in the present powder sizes. Although a non-polar dielectric with a low dielectric constant ($\varepsilon_r \approx 4$), SiO_2 polarizes to compensate for the difference in chemical potentials between the Cu and Al electrodes and itself, as shown in Figure 3, it is observed that at room

temperature (~20 °C), the first SKP runs of the Al/SiO_2/Cu cell, at OCV, and shows the SiO_2 surface chemical potential to bend linearly and compensate for the difference in chemical potentials at the SiO_2/Al more than at the SiO_2/Cu (Figure 3a,b). The difference in chemical potentials between the Al and the dielectric is higher than the difference with the Cu. The latter preconizes the usual description of the role of an insulator in a solid-state device such as a FET. However, as observed in Figure 3c–f, as the SKP scans follow, the dielectric starts to polarize, and in SiO_2, a positive–negative–positive polarization is then visible, as evident in Figure 3f for an experiment made with the Zn/SiO_2/Cu cell. The dielectric changes from a behavior typically related to its band structure, reflected in band bending, to dielectric polarization with the formation of positive–negative–positive charged regions, which may be associated with the larger dielectric polarization relaxation time and eventually to the temperature of 36 °C (Table 2). More energy is available to overcome the E_a, or the energy necessary for assuming a configuration that is not fully energetically favorable (Figures 2c and 3d).

A sharp potential step is shown on both Cu/SiO_2 and SiO_2/Al heterojunctions, corresponding to internal resistances at the interfaces. These internal resistances are likely to justify the lack of a continuous equalization of surface chemical potentials Cu/SiO_2/Al. For example, a heterojunction SiO_2/Al equalizes its surface chemical potential with Cu, as shown in Figure 3c–f and represented in Table 2 by Cu . . . SiO_2/Al and Zn/SiO_2 . . . Cu1 . . . Cu2. The alignment seems to be more likely to occur at the absolute potential of the Cu, which is expected, as Cu is the electrode more often connected to the SKP.

The surface chemical potentials of each metal and the SiO_2 are a little smaller (Physical scale, Figure 2b) when compared with the potentials obtained when the materials were analyzed and electrically insulated, as reported in [31].

The incapacity of making the metals' surface chemical potentials vary toward equalizing their chemical potential at the interface, and in its immediate vicinity, is likely due to the internal resistance at the interfaces and within the oxide. However, the alignment is made through the action of the electric field away from one of the interfaces (Figure 3d,e).

Dielectrics. MgO possesses the smallest work function studied, smaller than Al (Table 2). It aligns almost continuously its surface chemical potential with Al, mirroring the alignment of ZnO with Cu in [31]. There is a slightly positively charged MgO/Al interface region (Figure 4a,b). The more negatively charged side of the MgO points towards the Cu when the connection to the SKP is made through the Cu (Figure 4a,b), which is the behavior of an n-type semiconductor such as ZnO. In the experiment corresponding to Figure 4c,d, the opposite happens even when the Cu is connected to the SKP, showing the expected insulator band bending with no n-type semiconductor features. The MgO does not seem to show negative-positive-negative polarized regions either. In other words, the dielectric polarization does not seem to have an influence, although it might be possible that it accounts for the behavior in Figure 4a,b. A stiff step Cu/MgO in Figure 4a,b indicates high interfacial resistance, which poses difficulties in equalizing the surface chemical potentials at the interfaces. The positively charged spike in Figure 4a,b on the surface chemical potential of Al allows for the Cu/MgO . . . Al surface potentials equalization (~0.60 V) and likely demonstrates the Peregrine Rogue solitons described in [36,37].

Dielectrics. Li_2O has a work function with values in the interval between the Cu and the Al work functions. Therefore, it brings the surface chemical potential of the Al down when the Cu connects to the SKP, and it brings the Cu up when the Al is connected to the SKP, being able to exchange electrons with the instrument and keeping its chemical potential close to the one it shows when electrically insulated [31]. In both the latter configurations (Figure 5a–c), the Li_2O shows a p-type semiconductor behavior. As underlined previously, Li_2O is one of the most common SEI layer constituents that form in Li-ion batteries due to the equalization of the lithiated graphite with the liquid electrolyte electrochemical potential through electron tunneling from the graphite (LiC_6) to the LUMO (lowest unoccupied molecular orbital) of the electrolyte with lower energy (Physical scale, Figure 2b). The Li_2O then acts as a solid electrolyte, with the diffusion of Li^+-ions happening through it. This

latter behavior is in agreement with the p-type semiconductor behavior of the NASICON when connected to a resistor and of the LAGP at OCV and connected to a resistor, as observed herein.

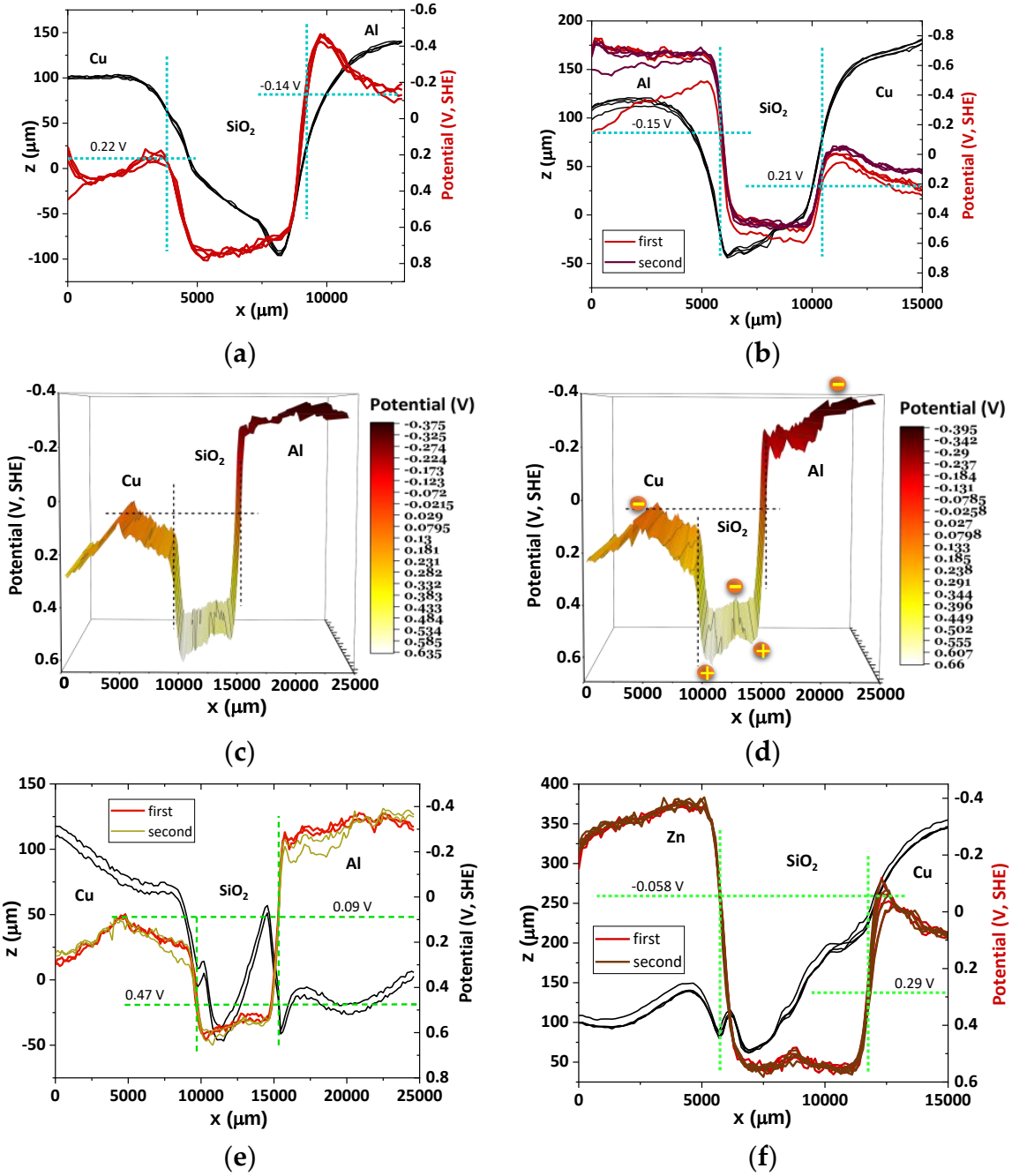

Figure 3. Topography and surface chemical potentials for an Al/SiO_2/Cu cell show different energies for the equalization of the surface chemical potentials of the heterojunctions Cu/SiO_2, SiO_2/Al, Al/SiO_2, and Zn/SiO_2: (**a**) straight band bending denoted by the SiO_2 surface chemical potential when Cu was connected to the SKP; (**b**) straight band bending denoted by the SiO_2 surface chemical potential when Al is connected to the SKP mirroring (**a**); (**c**–**e**) extended SKP analysis showing dielectric behavior of surface chemical potential of SiO_2 and a positive–negative–positive polarization distribution on the Cu that transitions almost seemingly to the SiO_2 polarized positive–negative–positive, and, finally, the Al positive-negative; (**f**) Zn/SiO_2/Cu with positive–negative–positive polarization of the dielectric (SiO_2).

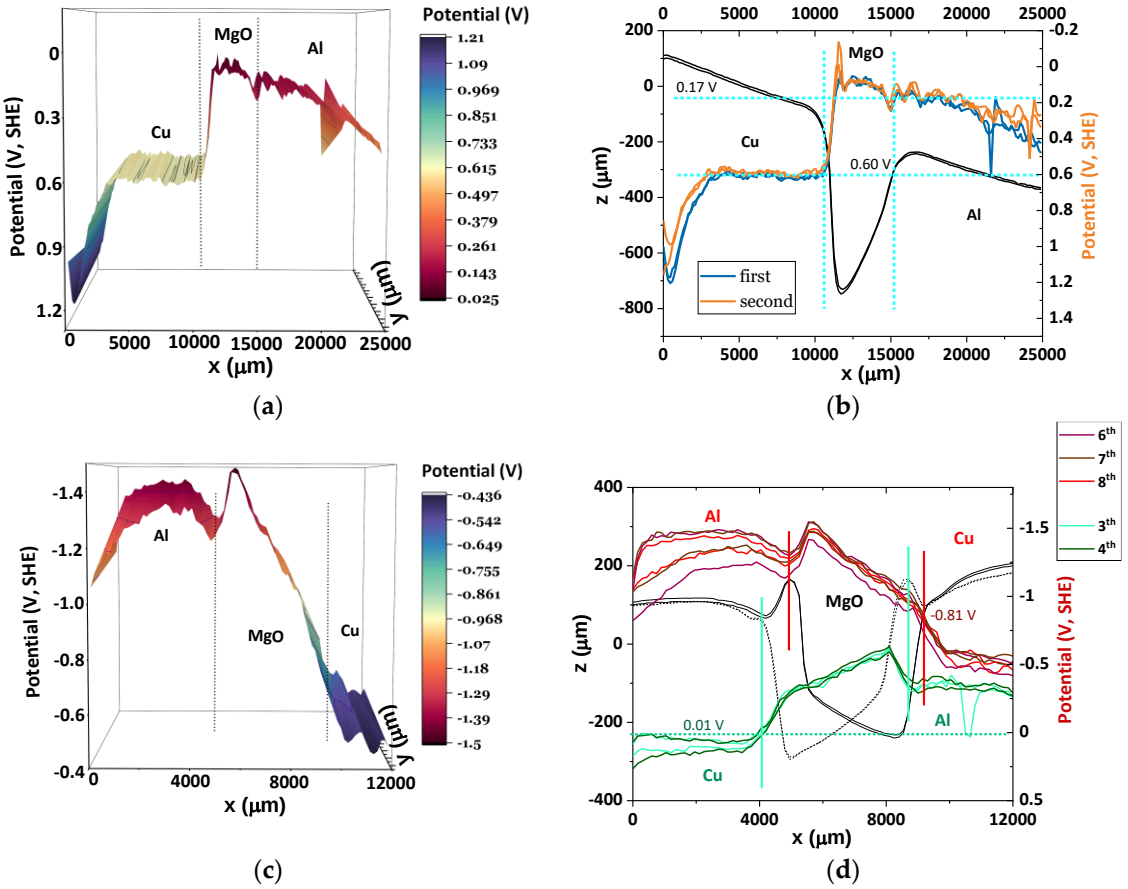

Figure 4. Topography and surface chemical potentials for an Al/MgO/Cu cell show different energies for the equalization of the surface chemical potentials of the heterojunctions Cu/MgO, MgO/Al, and Al/MgO: (**a**,**b**) extended SKP analyses showing n-type semiconductor band bending denoted by the surface chemical potential of MgO when Cu was connected to the SKP; equalization of Cu/MgO surface chemical potentials with the Al's is made through a positively polarized spike at the surface of the Al; (**c**) straight band bending denoted by the surface chemical potential of MgO when Al is connected to the SKP mirroring (**a**); (**d**) SKP analyses showing the differences for when the Al or the Cu are connected to the instrument. The electrode that is connected to the SKP is able to achieve similar surface chemical potentials to the absolute chemical potentials widely available in the literature represented by [38]; for example, Al reaches −1.45 V (SHE) in (**c**) for a tabulated value of −1.66 V (SHE) [38].

Although not showing as stiff interfacial resistances as previously demonstrated by SiO_2 and MgO, in the Cu/Li_2O/Al of Figure 5d, there is a step in potential energy at the Li_2O/Al heterojunction.

The electron localization function in Figure 5e, which was obtained for a (001) surface after optimization of the crystalline structure, shows delocalized electrons at the surface of the Li_2O. Whereas Li_2O is an insulator with an indirect gap of 5.286 eV, the surface states of the (001) surface show a metallic surface. It is noteworthy that Li_2O (Fm-3m) was analyzed and shown to be a trivial topologic insulator [39]. This property may be related to the solid electrolyte interphase (SEI) layer role of the Li_2O and allow battery cell interphase and interface tailoring (Figure 2a).

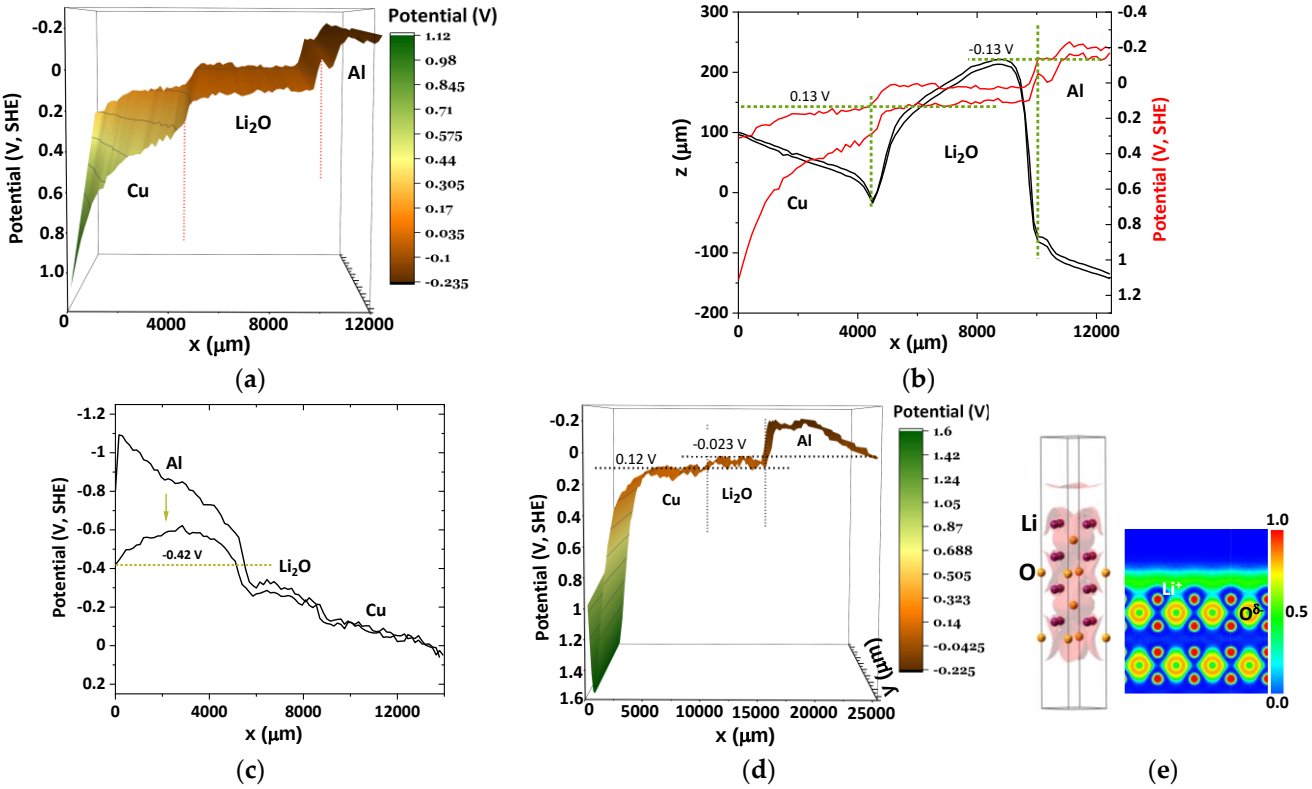

Figure 5. Topography and surface chemical potentials for an Al/Li_2O/Cu cell show slightly different energies for the equalization of the surface chemical potentials of the heterojunctions Cu/Li_2O and Li_2O/Al. (**a**,**b**) SKP analysis showing p-type semiconductor band bending of Li_2O when Cu was connected to the SKP; (**c**) p-type band bending observed in the surface potential of Li_2O when Al is connected to the SKP showing small interfacial resistance at both interfaces; (**d**) SKP extended analysis not showing a pronounced p-type semiconductor band bending but rather a flat surface chemical potential of Cu/Li_2O with a step toward the Al, reflecting internal interfacial resistance; (**e**) electron localization function (ELF): isosurface (3D) (ELF = 0.28) and slice (2D) showing delocalized electrons (ELF = 0.50) at the (001) surface of Li_2O.

Solid Electrolyte. $Na_3Zr_2Si_2PO_{12}$–NASICON is a solid-state electrolyte.

The solid electrolyte, $Na_{1+x}Zr_2Si_xP_{3-x}O_{12}$ known as NASICON, as reported previously, shows a rhombohedral phase (R-3c) between $0 \leq x \leq 3$, except $1.8 \leq x \leq 2.2$ [40] (SI, Introduction), where the monoclinic phase (C2/c) is stable at room temperature. The monoclinic C2/c phase, $Na_3Zr_2Si_2PO_{12}$, transforms into the rhombohedral R-3c phase in a gradual process as temperature increases and completes at ~150 °C [41].

In Figure 6a,b, the surface chemical potential of $Na_3Zr_2Si_2PO_{12}$ reflects a slight n-type band bending at OCV with an almost non-noticeable accumulation of electrons at the Cu/$Na_3Zr_2Si_2PO_{12}$ heterojunction and electron holes at the interface $Na_3Zr_2Si_2PO_{12}$/Al. When the circuit is closed by a resistor of 980 Ω, the Al surface opposed to the heterojunction with the NASICON increases its surface chemical potential with the electrons flowing from the negative electrode (Al) to the positive electrode (Cu) through the resistor. In a closed circuit, the band bending in $Na_3Zr_2Si_2PO_{12}$ configures a p-type semiconductor behavior, although it is much less pronounced, as observed in LAGP. It is noteworthy that NASICON shows an ionic conductivity of 10^{-4} S.cm^{-1} whereas LAGP shows > 10^{-3} S.cm^{-1} at room temperature. The latter property, the p-type semiconductor behavior, is likely related to the fast band bending promoted by the diffusion of the Li^+ ions towards the Cu while the cell is set to discharge. Another common property observed in the solid electrolytes studied in this work, and $Li_{2.99}Ba_{0.005}ClO$ shown in the supplement of [31], is the equalization of the surface chemical potentials of the two heterojunctions at the same potential; and,

whereas for $Li_{2.99}Ba_{0.005}ClO$, the surface potential of the electrodes equalizes with that of the heterojunctions towards the inner electrode, in NASICON and LAGP, there is a quantum barrier/well corresponding to an internal resistance at the interfaces, especially at the interface solid electrolyte/Al reflected in the cell by a very low OCV (10 to 34 mV) for a Cu//Al cell with expected $\Delta V_{OC} = \frac{\mu_{Al}-\mu_{Cu}}{e}(Physical\ scale) \approx 1.1$ V, having into account the SKP measured chemical potentials for electrically insulated materials. As with the other cells of the type $metal_1$/insulator/$metal_2$ studied so far, there is an emergency manifested in the equalization of the surface chemical potential of the electrodes and heterojunctions more frequently observed for the electrode connected to the SKP. The emergency also manifests as an extreme bending of the surface chemical potentials of the electrodes, especially if the electrode is Al.

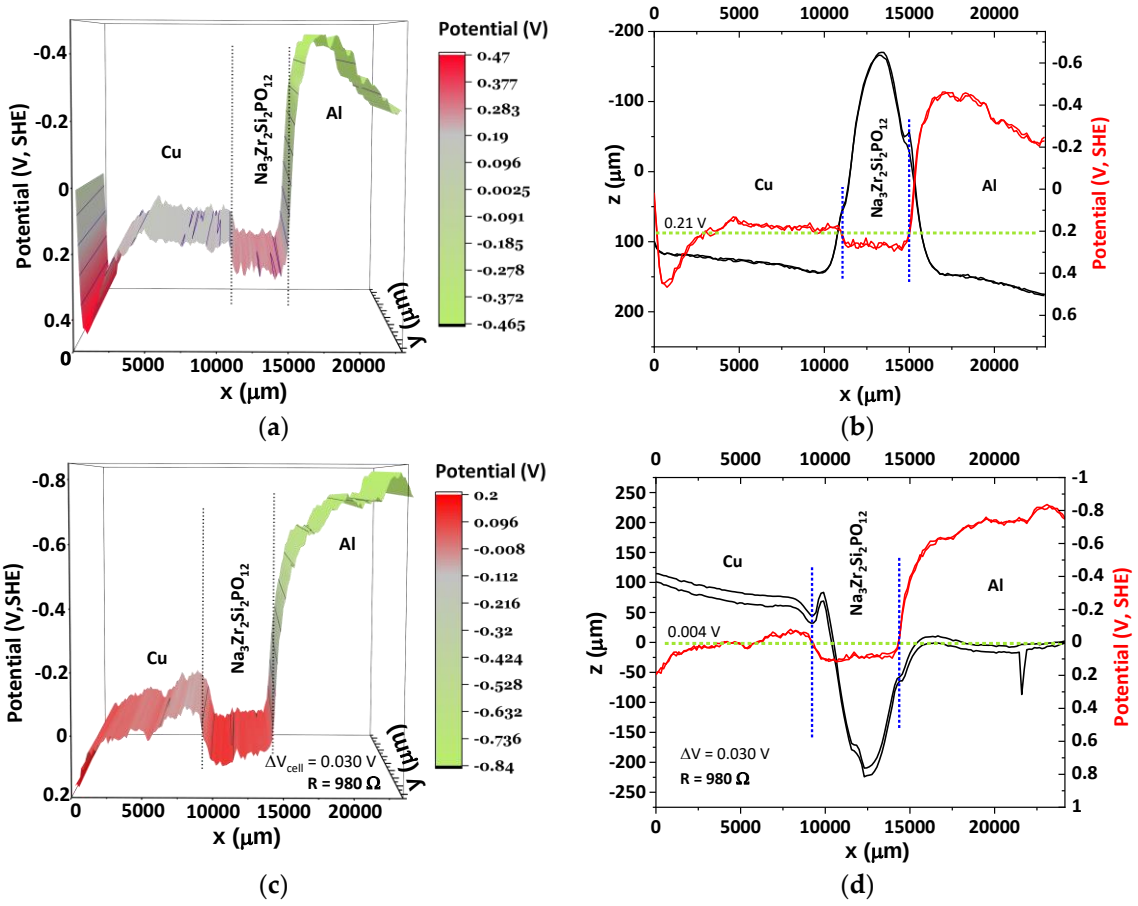

Figure 6. Topography and surface chemical potentials for an Al/$Na_3Zr_2Si_2PO_{12}$–NASICON/Cu cell show just one energy for the equalization of the surface chemical potentials for both heterojunctions; (**a**,**b**) SKP analysis showing a slight tendency from $Na_3Zr_2Si_2PO_{12}$ to perform as an n-type semiconductor with smooth band bending when Cu was connected to the SKP at OCV; the cell also shows the extreme bending of the Al surface chemical potential towards equalization of the surface chemical potentials not achieved up to 2.4 cm; (**c**,**d**) $Na_3Zr_2Si_2PO_{12}$ p-type band bending while the cell is set to discharge when a 980 Ω resistor was connected closing the circuit. A potential difference of 0.03 V was then obtained between Cu//Al. The difference in surface chemical potentials between OCV and the closed circuit relates to the electrodes bending surface chemical potential, which is much more extreme at OCV; $Na_3Zr_2Si_2PO_{12}$ behaves as an n-type semiconductor with small band bending towards the Al at OCV and as p-type while set to discharge with the resistor manifested by slight band bending towards the Cu; SKP extended analysis displaying a pronounced interfacial internal resistance at NASICON/Al. We highlight that these experiments were executed at <40 °C, and therefore, the configuration of the cell's surface chemical potentials at 50 °C—an optimal temperature for the performance of all-solid-state electrolytes in batteries—might differ.

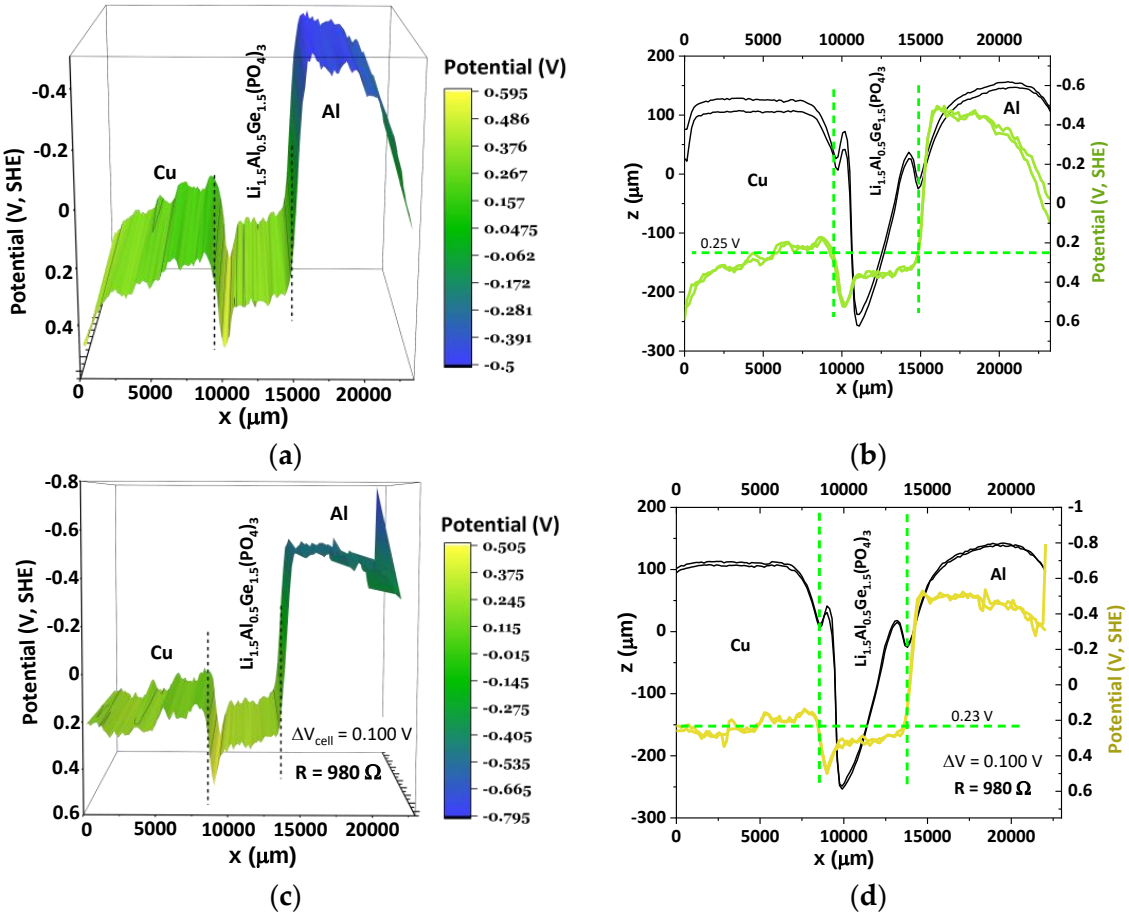

Figure 7. Topography and surface chemical potentials for an Al/$Li_{1.5}Al_{0.5}Ge_{1.5}(PO_4)_3$–LAGP/Cu cell show just one energy for the equalization of the surface chemical potentials for both heterojunctions, as observed with $Na_3Zr_2Si_2PO_{12}$; (**a**,**b**) SKP analysis showing clear p-type semiconductor band bending when Cu was connected to the SKP at OCV; they also show the extreme bending of the Al surface chemical potential towards equalization of the surface chemical potentials; (**c**,**d**) p-type band bending while almost showing no difference to the OCV configuration when a 980 Ω resistor was connected closing the circuit. A potential difference of 0.1 V was obtained between Cu//Al. The difference between OCV and the closed circuit relates to the electrodes bending. SKP extended analysis displaying a pronounced interfacial internal resistance at LAGP/Al. We highlight that these experiments were executed at <40 °C, and therefore, the configuration of the cell's surface chemical potentials at 50 °C—an optimal temperature for the performance of all-solid-state electrolytes in batteries—might differ.

Solid Electrolyte. $Li_{1.5}Al_{0.5}Ge_{1.5}(PO_4)_3$, NASICON type structure, hereafter LAGP, is a solid state electrolyte. According to [42,43], LAGP demonstrates a relatively high ionic conductivity of 4.2 $mS.cm^{-1}$ at room temperature. Furthermore, LAGP has an advantageous electrochemical stability window (1.8–7 V vs. Li^+/Li) [44–47]. Figure 7 shows SKP's surface chemical potentials for an Al/insulator/Cu cell with the insulator gap replaced by LAGP. A dielectric polarization with positive–negative–positive polarization regions was expected to be allowed by ion hopping; nevertheless, this was not what was observed. At OCV, the bending of the vacuum surface, a reflex of the bending of the E_C and E_V bands of LAGP, shows a p-type semiconductor behavior. The surface chemical potential of LAGP at the interface with Cu is lower than at the Al side, indicating a positive polarization near Cu, possibly by an accumulation of Li^+-ions. This is the same effect as observed at Li_2O/Cu as shown in Figure 5a–c. From the best of our knowledge, this is a new result and, as with the Li_2O, it indicates that the solid electrolyte shows an accumulation of Li^+-ions at the

interface of the positive electrode, at OCV, and with which the electrons and cathode's active material react while discharging with a resistor load (Figure 7c,d).

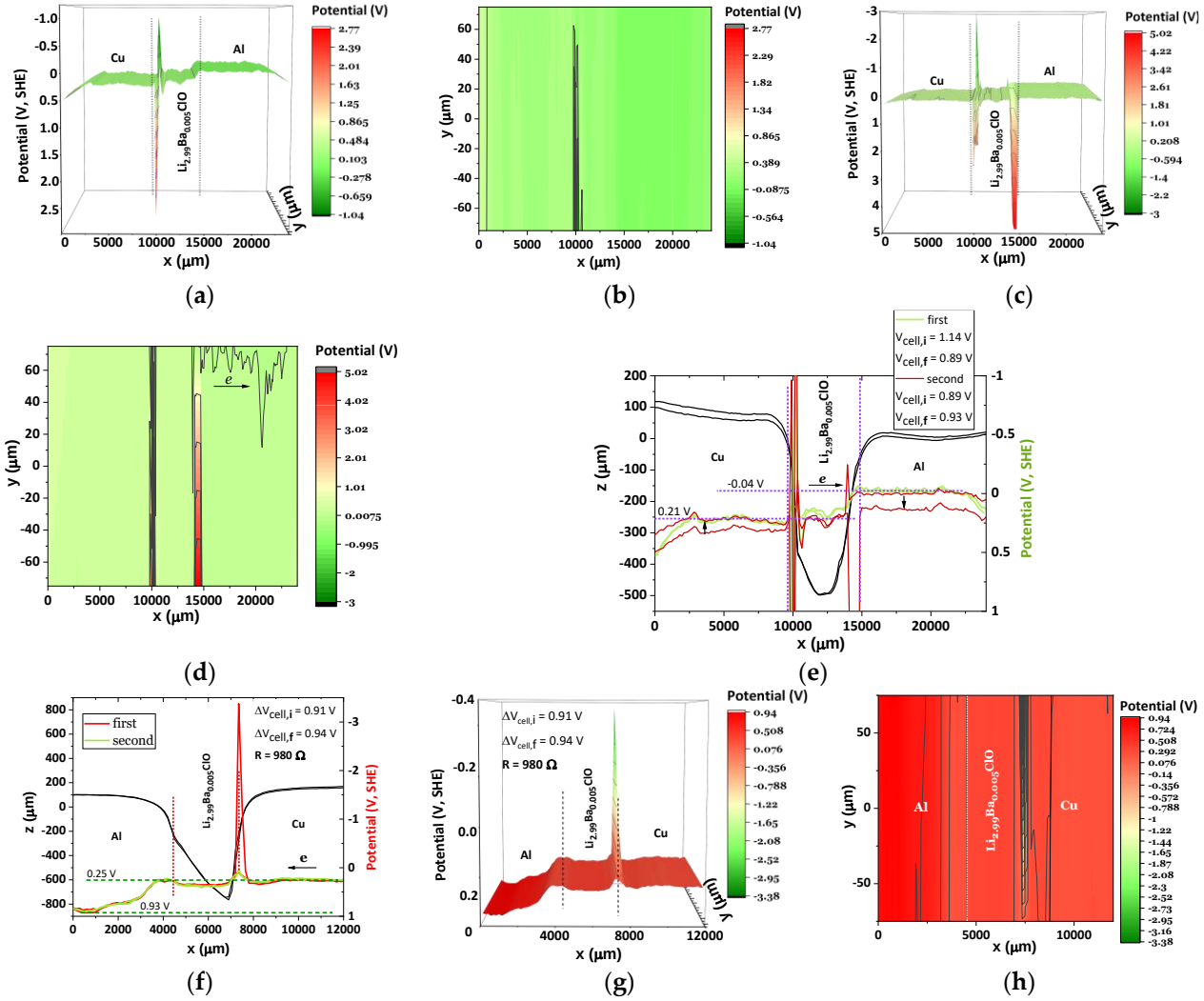

Figure 8. Topography and surface chemical potentials for an Al/$Li_{2.99}Ba_{0.005}ClO$ (Li^+-glass)/Cu cell; (**a**–**e**) SKP analysis showing evident propagation of the SPP parallel strips (solitons) from the Cu to the Al through the Li^+-glass surface; (**f**–**h**) show different perspectives of the propagation of a plasmon solitons from the Cu electrode at higher potential (Physical scale) to the Al electrode at lower potential through tunneling, diffusion, and drift, when the circuit is closed by a resistor load; the Al is the electrode in contact with the SKP; there is not a considerable variation of the surface chemical potential of the Cu, but the Al dropped down to +0.93 V (SHE).

If the electrolyte shows other dielectric capabilities, then they likely happen at T > 36 °C, where the activation energy of more ions is overcome, and more Li^+-ions hop faster.

A very clear bending of the Al surface chemical potentials, as well as the Cu's at OCV, makes it possible to observe an equilibrium Cu1 . . . Cu2/LAGP/Al1 . . . Al2 within the extended cell (Table 2, Figure 7a,b). This latter value of the potential energy for all the materials of the cell may correspond to the Fermi level (Figures 2d and 7). A significant interfacial resistance at the LAGP/Al interface, or potential barrier/well as discussed in [31], is characterized by a sharp step down of the surface chemical potential and may justify the difference between the expected OCV for a Cu//Al cell 1.1 V and the OCV obtained for Cu/LAGP/Al of 0.09 V (Table 2) [31].

When the Cu/LAGP/Al cell is connected to a 980 Ω resistor, the surface chemical potentials of the electrodes closer to the cell's edges bend up upon electron circulation

through the external circuit. The surface chemical potential of the Al grows at the border (Physical scale, Figure 2b) to a value that is much closer to the insulated Al SKP value; in other words, the work function decreases. Other features that seem rather consistent are the solitons or the surface plasma polaritons (SPP) wave-like behavior on the Cu electrode due to the Cu/LAGP contact.

The internal resistance, corresponding to potential barriers or wells, expressed in a step down of the surface chemical potentials at the interfaces metal/dielectric and metal/LAGP solid electrolyte, is responsible for very low OCVs and very high impedance. A high dielectric or solid electrolyte impedance favors straight band bending and n-type or p-type semiconductor-like behavior at room temperature instead of alternate dielectric polarization, which is achieved through higher mobility of the ions.

It is highlighted that LAGP's granulometry is much smaller than NASICON's, which may reflect on the internal impedance and not as much on the surface transport phenomena.

Solid electrolyte and ferroelectric. $Li_{2.99}Ba_{0.005}ClO$, herein *Li^+-glass*, is a ferroelectric. Figure 8a–e shows the beginning of a flipping process that occurs between the Cu and Al's surface chemical potential mediated by the Li^+-glass. In Figure 8a,b, at the Cu/Li^+-glass heterojunction, negatively charged plasmons alternate with positively charged, initiating their transport through the surface of the Li^+-glass. Figure 8c–e show tunneling to the Al mediated through a positively charged plasmon soliton. It is noteworthy that at the end of the second cycle, self-charge had already occurred (ΔV = 0.14 V), and the Al surface chemical potential had visibly decreased whereas the Cu's had increased (Physical scale, Figure 2b). Figure 8f–h show what the subsequent process is, where the Al surface chemical potential drops, equalizing the Cu's and negatively charged plasmon solitons parallel to the interfaces (y-axis), traveling along the x-axis from the Cu to the Al electrode, and closing the feedback circuit through the inner cell (through the surface of the ferroelectric) [48]. Coherent plasmons tunnel from the Li^+-glass to the Al electrode after tunneling from the Cu to the ferroelectric and propagating through its surface.

By performing cyclic voltammetry I-V (Figure 9a), it is possible to determine that after the SKP experiment, the cell remains polarized, presenting a current of 0.08 to 0.100 mA, at OCV, and after SKP analyses ($0.77 \leq V_{OC}(V) \leq 1.04$). The internal resistance, $R_2 = 2.2 \times 10^6\ \Omega$ (Figure 9b), corresponds to a conductivity through the surface of Li^+-glass of $2.4 \times 10^{-7}\ S{\cdot}cm^{-1}$. It is noteworthy to highlight that semiconductors have conductivities between 10^{-8} and $10^2\ S{\cdot}cm^{-1}$, and the powders corresponding to a 5.5 mm thick layer of $Li_{2.99}Ba_{0.005}ClO$ had diameters with μm-sizes and were relatively loose in the space between metals; the pressure exerted to contain the powders was manual and made with a spatula-like tool and, therefore, the real conductivity of the Li^+-glass surface is much high than measured.

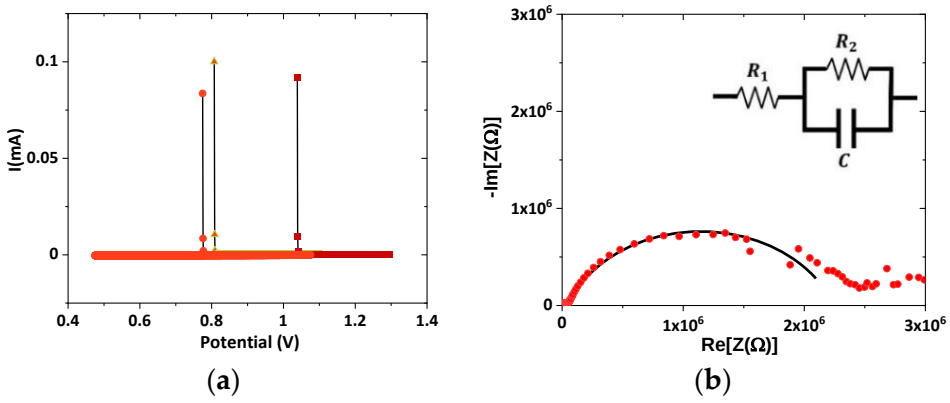

Figure 9. Cyclic voltammetry (CV) and impedance spectroscopy (EIS) for an Al/$Li_{2.99}Ba_{0.005}ClO$ (Li^+-glass)/Cu cell. (**a**) I-V plots (2 $mV{\cdot}s^{-1}$) showing initial polarization of 0.08 to 0.100 mA, at 25 °C, after SKP analyses ($0.77 \leq V_{OC}(V) \leq 1.04$); (**b**) EIS plot showing the impedance of the cell at 25 °C; $R_2 = 2.2 \times 10^6\ \Omega$ corresponding to a conductivity through the surface of Li^+-glass of $2.4 \times 10^{-7}\ S{\cdot}cm^{-1}$.

The Al/$Li_{2.99}Ba_{0.005}ClO$ (Li^+-glass)/Cu cell was the only one to show a potential difference that approximates the theoretical of 1.1 V; although due to the thick layer of ferroelectric electrolyte powder (5.5 mm) within the cell, with μm diameters manually pressed together, a much higher resistance was expected in the face of what was observed with the oxides and other solid electrolytes.

The self-charge happening even when the cell is connected to a resistor load is likely due to the inversion in surface chemical potentials of the electrodes while not manifesting an inversion of the bulk chemical potentials. This inversion enables drift-like plasmonic conduction in feedback through the surface of the electrolyte, enabling, therefore, self-charge. Previous results with ferroelectric electrolytes of the family $A_{3-2x}M_xClO$ (A = Li, Na, K) show that the conduction of electrons through the surface is observed in hermetically closed pouch cells [26] and coaxial cells [49,50], leading to self-cycling and self-charging.

Ab initio simulations. Finally, Figures 10 and 11 show the ab initio simulations of the surfaces with subsequent calculations of the work functions of the electrode metals, dielectric oxides, and solid electrolytes. All the results are in good agreement with the experiments (Table 2) except the Al (Figure 10b), which is able to vary its surface chemical potential through a wide range of values from −1.5 V, SHE (Figure 4c) to 0.60 V, SHE (Figure 4b). In [31], we show Al's chemical surface potential to vary to +5 V (SHE).

It is noteworthy that we have simulated the electronic band structure for NASICON and LAGP (Figure 11a,c) because the materials are disordered, and therefore, they assume different possible structures. That is perhaps a reason contributing to LAGP electronic band structure not being widely accessible in the literature. For comparison, the structure of NASICON was also simulated.

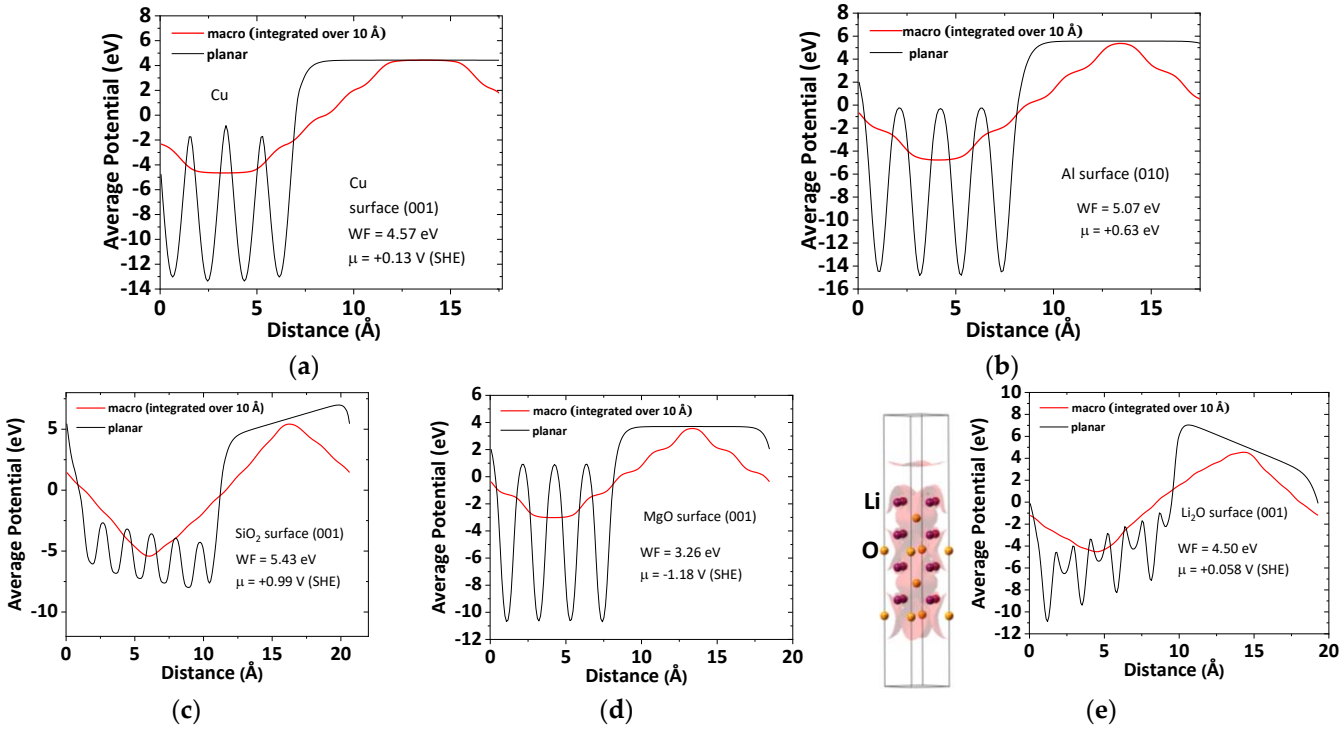

Figure 10. *Ab initio*: average potentials for metal electrodes and dielectrics were obtained after the simulation of the corresponding surfaces after optimization of the corresponding crystal structures. The macro potentials correspond to integration over 10 Å; (**a**) for (001) simulated surface of Cu, and (**b**) for (010) simulated surface of Al; for (001) simulated surfaces of (**c**) SiO_2; (**d**) MgO; (**e**) Li_2O. ***Note:*** The (001) surface average potential for Al was obtained in [31].

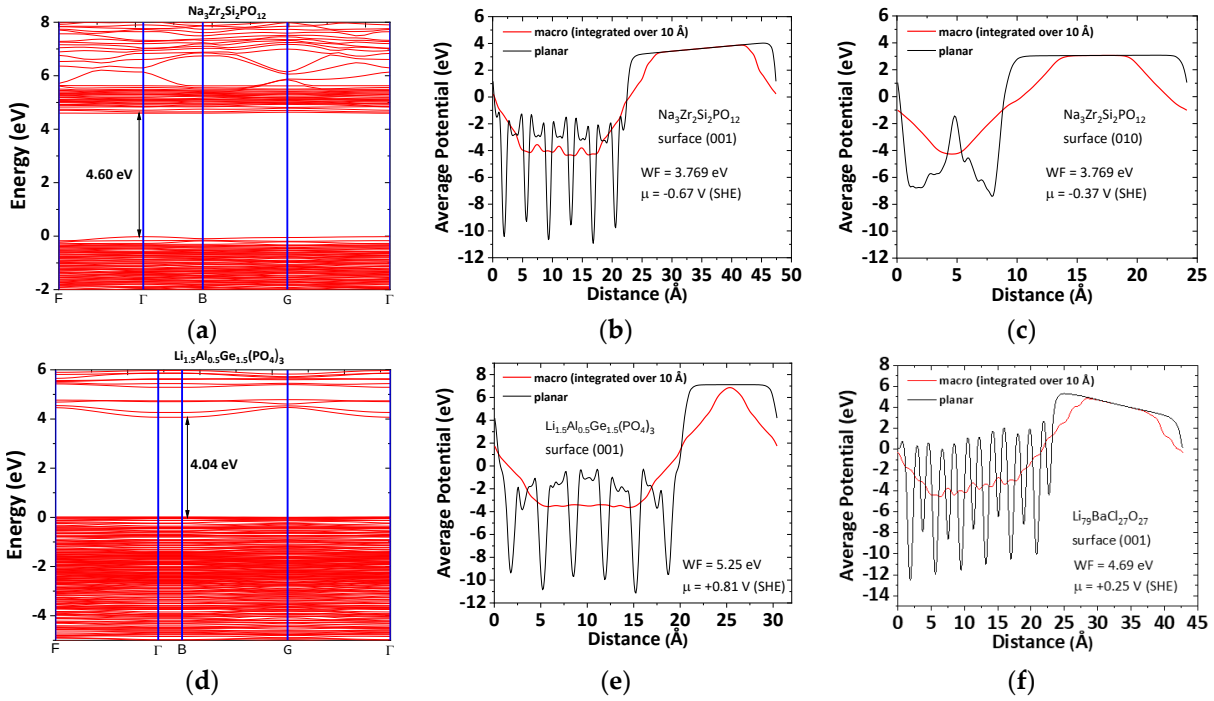

Figure 11. *Ab initio*: average potentials for solid electrolytes. The macro potentials correspond to integration over 10 Å; average potentials for (001) simulated surfaces and (**a**) electronic band structure of $Na_3Zr_2Si_2PO_{12}$ showing a band gap of 4.60 eV, obtained for the bulk superstructure (P1) using DFT; (**b**) average potentials for the (001) and (010) simulated surfaces of $Na_3Zr_2Si_2PO_{12}$; (**c**) electronic band structure of $Li_{1.5}Al_{0.5}Ge_{1.5}(PO_4)_3$ showing a band gap of 4.04 eV, obtained for the bulk superstructure (P1) using DFT; average potentials for (001) simulated surface of (**d**) $Na_3Zr_2Si_2PO_{12}$; (**e**) $Li_{1.5}Al_{0.5}Ge_{1.5}(PO_4)_3$; (**f**) $Li_{2.99}Ba_{0.005}ClO$ ($Li_{79}BaCl_{27}O_{27}$) ***Note:*** The (001) surface average potential for Al was obtained in [31]; the electronic band structures for $Na_3Zr_2Si_2PO_{12}$ and $Li_{1.5}Al_{0.5}Ge_{1.5}(PO_4)_3$ were calculated for triclinic (P1) as these phases are disordered, and therefore have to be simulated in a superstructure although respecting atom positions, cell volume and shape.

5. Conclusions

This work aimed to show the differences between dielectric oxides and solid electrolytes, and among solid electrolytes, a ferroelectric electrolyte. It was not expected that a cell with hyperbolic dimensions could highlight these many differences.

Surface chemical potentials: the most impressive feature is that no matter what dielectric/solid electrolyte disjoints the two electrode metals, the surface chemical potential equalizes throughout a ~2.5 cm thickness cell due to the propagation of the electric field throughout the cell.

Surface chemical potentials of the metal electrodes: the metals have an unexpectedly high capacity to bend their surface chemical potentials and to propagate SPP solitons.

Surface chemical potentials of the insulators: the surface chemical potentials seem to be much more affected by the insulator that disjoints the two metal electrodes than the surface preparation or texture; they do not appear to depend too much on the particle size either. However, the particle size should influence the cell's impedance.

Dielectric materials: SiO_2, MgO, and Li_2O may bend their surface chemical potential straight with the more negatively charged part closer to the negative electrode (Al), which is at a higher chemical potential than the positive (Cu). However, they can assume other configurations, such as those of an n-type (MgO) or p-type (Li_2O) semiconductor.

Solid electrolytes: NASICON tends to polarize as an n-type semiconductor at OCV and as a p-type in a closed circuit, whereas LAGP polarizes as a p-type both at OCV and in a closed circuit with a resistive load.

Differences in dielectrics vs. *solid-electrolytes:* the difference between the LAGP and the previous dielectrics is that positive charge accumulates close to the interface with Cu creating a difference of 0.15 V over 630 μm; there is no considerable polarization of the LAGP surface potential on the Al side. It is likely that Li^+-ions are just accumulated at the Cu side and not on the Al side, as the relative work functions would determine. The discharge reaction (spontaneous) happens at the positive electrode, with Li^+ being delivered from the electrolyte and the electrons from the external circuit, which is in agreement with the surface chemical potentials observed with LAPG. This might be a common feature of solid electrolytes that do not accumulate being ferroelectric, which superimposes the condition of being a solid electrolyte.

The equalization of the surface chemical potentials of all the solid electrolytes, including the ferroelectrics, is made at both interfaces at the same energy, immediately or after the transient state, which to the best of our knowledge, is yet another novel result.

Ferroelectric solid electrolyte: The ferroelectric electrolyte, Li^+-glass, is the only one capable of achieving electrical potentials that are close to the theoretical potentials (1.1 V) in a 5.5 mm gap cell, showing surface plasmon phenomena with micro to millimeter wavelengths correspondent to THz frequencies attributed to electronic phenomena, and capable of closing the positive feedback discharge/self-charge. The ferroelectric electrolyte is the only one that is able to invert the surface chemical potentials of negative and positive electrodes and yet store electrical energy without reverting the polarization of the cell.

Finally, ionic conductivity seems to have an important role as the efficiency of the cells with solid electrolytes increases with ionic conductivity. However, the dielectric constant follows the same trends as ionic conductivity, indicating that it is related to ionic conductivity in solid electrolytes and, generally, the most accurate indicator also present for dielectrics.

The present findings may have applications in batteries, capacitors, photovoltaics, thermo-electrics, transistors, metamaterials, and topologic insulators but also in novel device architectures that may harvest energy through topologic plasmonic feedback while storing it.

Supplementary Materials: The following supporting information can be downloaded at: https://www.mdpi.com/article/10.3390/batteries8110232/s1, Review on the dielectrics and solid electrolytes studied herein. References [51–150] are cited in the Supplementary Materials.

Author Contributions: Cell fabrication and experiments: A.N.G.; review of state of the art: A.N.G., B.A.M., H.K. and M.C.B.; original ideas and draft, formal analysis, simulations, and supervision: M.H.B.; review and editing: All. All authors have read and agreed to the published version of the manuscript.

Funding: This research was funded by the CAVALI project, reference POCI-01-0247-FEDER-047728, co-funded by the ERDF, through the COMPETE 2020, under the PORTUGAL 2020 Partnership Agreement; the Portuguese Foundation for Science and Technology FCT UIDP/50022/2020 Emerging Technologies–LAETA, and PTDC/QUI-ELT/2593/2021 "Redox-active Metal-Organic Frameworks as Electrode Materials for Lithium-Ion Batteries" projects. B.A.M. thanks the "FLY.PT—Mobilize the Portuguese aviation industry to disrupt the future urban air transport" project, co-financed by the European Regional Development Fund (ERDF) through Portugal 2020. H.K. thanks the project ALBATTS ERASMUS+ 612675-EPP-1-2019-1-SE-EPPKA2-SSA-B co-funded by the Erasmus Program of the European Union.

Data Availability Statement: The data that support the findings of this study are available from the corresponding author upon reasonable request.

Acknowledgments: M.H.B. acknowledges John B. Goodenough's endowment to the MatER–Materials for Energy Research lab, FEUP.

Conflicts of Interest: The authors declare no conflict of interest.

References

1. Lewis, N.S.; Nocera, D.G. Powering the planet: Chemical challenges in solar energy utilization. *Proc. Natl. Acad. Sci. USA* **2006**, *103*, 15729–15735. [CrossRef]
2. Liu, Y.; Li, Y.; Wu, Y.; Yang, G.; Mazzarella, L.; Procel-Moya, P.; Tamboli, A.C.; Weber, K.; Boccard, M.; Isabella, O.; et al. High-Efficiency Silicon Heterojunction Solar Cells: Materials, Devices and Applications. *Mater. Sci. Eng. R Rep.* **2020**, *142*, 100579. [CrossRef]
3. Eshetu, G.G.; Zhang, H.; Judez, X.; Adenusi, H.; Armand, M.; Passerini, S.; Figgemeier, E. Production of high-energy Li-ion batteries comprising silicon-containing anodes and insertion-type cathodes. *Nat. Commun.* **2021**, *12*, 5459. [CrossRef]
4. Saini, P.; Gidwani, L. An investigation for battery energy storage system installation with renewable energy resources in distribution system by considering residential, commercial and industrial load models. *J. Energy Storage* **2022**, *45*, 103493. [CrossRef]
5. Chen, Y.; Kang, Y.; Zhao, Y.; Wang, L.; Liu, J.; Li, Y.; Liang, Z.; He, X.; Li, X.; Tavajohi, N.; et al. A review of lithium-ion battery safety concerns: The issues, strategies, and testing standards. *J. Energy Chem.* **2021**, *59*, 83–99. [CrossRef]
6. Wen, J.; Yu, Y.; Chen, C. A Review on Lithium-Ion Batteries Safety Issues: Existing Problems and Possible Solutions. *Mater. Express* **2012**, *2*, 197–212. [CrossRef]
7. Lee, S.; Manthiram, A. Can Cobalt Be Eliminated from Lithium-Ion Batteries? *ACS Energy Lett.* **2022**, *7*, 3058–3063. [CrossRef]
8. Ma, S.; Jiang, M.; Tao, P.; Song, C.; Wu, J.; Wang, J.; Deng, T.; Shang, W. Temperature effect and thermal impact in lithium-ion batteries: A review. *Prog. Nat. Sci. Mater. Int.* **2018**, *28*, 653–666. [CrossRef]
9. Hoffmann, M.; Salahuddin, S. Ferroelectric gate oxides for negative capacitance transistors. *MRS Bull.* **2021**, *46*, 930–937. [CrossRef]
10. Balandin, A.A.; Kargar, F.; Salguero, T.T.; Lake, R.K. One-dimensional van der Waals quantum materials. *Mater. Today* **2022**, *55*, 74–91. [CrossRef]
11. Sekine, A.; Nomura, K. Axion electrodynamics in topological materials. *J. Appl. Phys.* **2021**, *129*, 141101. [CrossRef]
12. Smirnova, D.; Leykam, D.; Chong, Y.; Kivshar, Y. Nonlinear topological photonics. *Appl. Phys. Rev.* **2020**, *7*, 021306. [CrossRef]
13. Guo, Y.; Qu, X.; Hu, Z.; Zhu, J.; Niu, W.; Liu, X. Highly elastic and mechanically robust polymer electrolytes with high ionic conductivity and adhesiveness for high-performance lithium metal batteries. *J. Mater. Chem. A* **2021**, *9*, 13597–13607. [CrossRef]
14. Kurzina, E.A.; Stenina, I.A.; Dalvi, A.; Yaroslavtsev, A.B. Synthesis and Ionic Conductivity of Lithium Titanium Phosphate-Based Solid Electrolytes. *Inorg. Mater.* **2021**, *57*, 1035–1042. [CrossRef]
15. Gupta, M.K.; Mittal, R.; Kumar, S.; Singh, B.; Jalarvo, N.H.; Delaire, O.; Shukla, R.; Achary, S.N.; Kolesnikov, A.I.; Tyagi, A.K.; et al. Stoichiometric tuning of lattice flexibility and Na diffusion in NaAlSiO4: Quasielastic neutron scattering experiment andab initiomolecular dynamics simulations. *J. Mater. Chem. A* **2021**, *9*, 16129–16136. [CrossRef]
16. Braga, M.H.; Oliveira, J.E.; Kai, T.; Murchison, A.J.; Bard, A.J.; Goodenough, J.B. Extraordinary Dielectric Properties at Heterojunctions of Amorphous Ferroelectrics. *J. Am. Chem. Soc.* **2018**, *140*, 17968–17976. [CrossRef] [PubMed]
17. Iqbal, S.; Bahadur, A.; Saeed, A.; Zhou, K.; Shoaib, M.; Waqas, M. Electrochemical performance of 2D polyaniline anchored CuS/Graphene nano-active composite as anode material for lithium-ion battery. *J. Colloid Interface Sci.* **2017**, *502*, 16–23. [CrossRef] [PubMed]
18. Bahadur, A.; Iqbal, S.; Shoaib, M.; Saeed, A. Electrochemical study of specially designed graphene-Fe3O4-polyaniline nanocomposite as a high-performance anode for lithium-ion battery. *Dalt. Trans.* **2018**, *47*, 15031–15037. [CrossRef]
19. Yang, L.; Wang, H.; Zhang, X.; Li, Y.; Chen, X.; Xu, X.; Zhao, X.; Song, A. Thermally Evaporated SiO Serving as Gate Dielectric in Graphene Field-Effect Transistors. *IEEE Trans. Electron Devices* **2017**, *64*, 1846–1850. [CrossRef]
20. Posadas, A.; Walker, F.J.; Ahn, C.H.; Goodrich, T.L.; Cai, Z.; Ziemer, K.S. Epitaxial MgO as an alternative gate dielectric for SiC transistor applications. *Appl. Phys. Lett.* **2008**, *92*, 233511. [CrossRef]
21. Smith, J.G.; Naruse, J.; Hiramatsu, H.; Siegel, D.J. Intrinsic Conductivity in Magnesium–Oxygen Battery Discharge Products: MgO and MgO_2. *Chem. Mater.* **2017**, *29*, 3152–3163. [CrossRef]
22. Lorger, S.; Usiskin, R.; Maier, J. Transport and Charge Carrier Chemistry in Lithium Oxide. *J. Electrochem. Soc.* **2019**, *166*, A2215. [CrossRef]
23. Tiliakos, A.; Iordache, M.; Marinoiu, A. Ionic Conductivity and Dielectric Relaxation of NASICON Superionic Conductors at the Near-Cryogenic Regime. *Appl. Sci.* **2021**, *11*, 8432. [CrossRef]
24. Wang, H.; Zhao, G.; Wang, S.; Liu, D.; Mei, Z.; An, Q.; Jiang, J.; Guo, H. Enhanced ionic conductivity of a $Na_3Zr_2Si_2PO_{12}$ solid electrolyte with Na_2SiO_3 obtained by liquid phase sintering for solid-state Na^+ batteries. *Nanoscale* **2022**, *14*, 823–832. [CrossRef] [PubMed]
25. Campanella, D.; Belanger, D.; Paolella, A. Beyond garnets, phosphates and phosphosulfides solid electrolytes: New ceramic perspectives for all solid lithium metal batteries. *J. Power Sources* **2021**, *482*, 228949. [CrossRef]
26. Braga, M.H.; Oliveira, J.E.; Murchison, A.J.; Goodenough, J.B. Performance of a ferroelectric glass electrolyte in a self-charging electrochemical cell with negative capacitance and resistance. *Appl. Phys. Rev.* **2020**, *7*, 011406. [CrossRef]
27. Braga, M.H.; Ferreira, J.A.; Murchison, A.J.; Goodenough, J.B. Electric Dipoles and Ionic Conductivity in a Na+ Glass Electrolyte. *J. Electrochem. Soc.* **2017**, *164*, A207. [CrossRef]
28. Braga, M.H.; Ferreira, J.A.; Stockhausen, V.; Oliveira, J.E.; El-Azab, A. Novel Li_3ClO based glasses with superionic properties for lithium batteries. *J. Mater. Chem. A* **2014**, *2*, 5470–5480. [CrossRef]

29. Zisman, W.A. A new method of measuring contact potential differences in metals. *Rev. Sci. Instrum.* **1932**, *3*, 367–370. [CrossRef]
30. Reiss, H. The Fermi level and the redox potential. *J. Phys. Chem.* **1985**, *89*, 3783–3791. [CrossRef]
31. Guerreiro, A.N.; Baptista, M.; Maia, B.; Braga, M.H. Interfacial chemistry with ZnO: In operando work functions in hetero cells. *ACS Appl. Energy Mater.* **2022**, *5*, 9811–9822. [CrossRef]
32. Kresse, G.; Furthmüller, J. Efficient iterative schemes for ab initio total-energy calculations using a plane-wave basis set. *Phys. Rev. B* **1996**, *54*, 11169–11186. [CrossRef] [PubMed]
33. Han, J.; He, M.; Yang, M.; Han, Q.; Wang, F.; Zhong, F.; Xu, M.; Li, Q.; Zhu, H.; Shan, C.; et al. Light-modulated vertical heterojunction phototransistors with distinct logical photocurrents. *Light Sci. Appl.* **2020**, *9*, 167. [CrossRef]
34. Maier, S.A. *Electromagnetics of Metals*; Plasmonics: Fundamentals and Applications; Springer: New York, NY, USA, 2007.
35. Zhang, H.Q.; Chen, F. Rogue waves for the fourth-order nonlinear Schrödinger equation on the periodic background. *Chaos An Interdiscip. J. Nonlinear Sci.* **2021**, *31*, 023129. [CrossRef] [PubMed]
36. Ye, Y.; Bu, L.; Wang, W.; Chen, S.; Baronio, F.; Mihalache, D. Peregrine Solitons on a Periodic Background in the Vector Cubic-Quintic Nonlinear Schrödinger Equation. *Front. Phys.* **2020**, *8*, 510. [CrossRef]
37. Shnir, Y.M. Chains of Interacting Solitons. *Symmetry* **2021**, *13*, 284. [CrossRef]
38. Trasa'tti, S. The absolute electrode potential: An explanatory note (Recommendations 1986). *Pure Appl. Chem.* **1986**, *58*, 955–966. [CrossRef]
39. Vergniory, M.G.; Wieder, B.J.; Elcoro, L.; Parkin, S.S.P.; Felser, C.; Bernevig, B.A.; Regnault, N. All topological bands of all nonmagnetic stoichiometric materials. *Science* **2022**, *376*, eabg9094. [CrossRef]
40. An, J.; Oh, S.; He, L.; Plewa, A.; Morita, M.; Zhao, Y.; Sakamoto, T.; Song, X.; Zhai, W.; Zeng, K.; et al. Composite NASICON ($Na_3Zr_2Si_2PO_{12}$) Solid-State Electrolyte with Enhanced Na + Ionic Conductivity: Effect of Liquid Phase Sintering. *ACS Appl. Mater. Interfaces* **2019**, *11*, 40125–40133. [CrossRef]
41. Lalère, F.; Leriche, J.B.; Courty, M.; Boulineau, S.; Viallet, V.; Masquelier, C.; Seznec, V. An all-solid state NASICON sodium battery operating at 200 °C. *J. Power Sources* **2014**, *247*, 975–980. [CrossRef]
42. Thokchom, J.S.; Kumar, B. Composite effect in superionically conducting lithium aluminium germanium phosphate based glass-ceramic. *J. Power Sources* **2008**, *185*, 480–485. [CrossRef]
43. Thokchom, J.S.; Gupta, N.; Kumar, B. Superionic Conductivity in a Lithium Aluminum Germanium Phosphate Glass–Ceramic. *J. Electrochem. Soc.* **2008**, *155*, A915. [CrossRef]
44. Leo, C.J.; Chowdari, B.V.R.; Rao, G.V.S.; Souquet, J.L. Lithium conducting glass ceramic with Nasicon structure. *Mater. Res. Bull.* **2002**, *37*, 1419–1430. [CrossRef]
45. Feng, J.K.; Yan, B.G.; Liu, J.C.; Lai, M.O.; Li, L. All solid state lithium ion rechargeable batteries using NASICON structured electrolyte. *Mater. Technol.* **2013**, *8*, 276–279. [CrossRef]
46. Meesala, Y.; Chen, C.Y.; Jena, A.; Liao, Y.K.; Hu, S.F.; Chang, H.; Liu, R.S. All-Solid-State Li-Ion Battery Using $Li_{1.5}Al_{0.5}Ge1.5(PO_4)_3$ As Electrolyte Without Polymer Interfacial Adhesion. *J. Phys. Chem. C* **2018**, *122*, 14383–14389. [CrossRef]
47. Xu, X.; Wen, Z.; Wu, X.; Yang, X.; Gu, Z. Lithium Ion-Conducting Glass–Ceramics of $Li_{1.5}Al_{0.5}Ge_{1.5}(PO_4)_3$–$xLi_2O$ (x = 0.0–0.20) with Good Electrical and Electrochemical Properties. *J. Am. Ceram. Soc.* **2007**, *90*, 2802–2806. [CrossRef]
48. Braga, M.H. Coherence in the Ferroelectric A3ClO (A = Li, Na) Family of Electrolytes. *Materials* **2021**, *14*, 2398. [CrossRef]
49. Danzi, F.; Valente, M.; Terlicka, S.; Braga, M.H. Sodium and potassium ion rich ferroelectric solid electrolytes for traditional and electrode-less structural batteries. *APL Mater.* **2022**, *10*, 031111. [CrossRef]
50. Danzi, F.; Camanho, P.P.; Braga, M.H. An All-Solid-State Coaxial Structural Battery Using Sodium-Based Electrolyte. *Molecules* **2021**, *26*, 5226. [CrossRef]
51. Eränen, S.; Törmä, P.; Gonzalez, P.; Rottenberg, X.; Puurunen, R.L.; Putkonen, M.; Vogl, A.; Tyholdt, F.; Tofteberg, H.; Muralt, P.; et al. Thin Films on Silicon. In *Handbook of Silicon Based MEMS Materials and Technologies*, 2nd ed.; Elsevier Inc.: Amsterdam, The Netherlands, 2015; pp. 124–205. [CrossRef]
52. Dionisio, K.L.; Phillips, K.; Price, P.S.; Grulke, C.M.; Williams, A.; Biryol, D.; Hong, T.; Isaacs, K.K. The Chemical and Products Database, a resource for exposure-relevant data on chemicals in consumer products. *Sci. Data* **2018**, *5*, 180125. [CrossRef] [PubMed]
53. Munteanu, D.; Autran, J. Modeling of energy bands in ultra-thin layer quantum nanostructures for solar cell applications. *J. Non-Cryst. Solids* **2011**, *357*, 1884–1887. [CrossRef]
54. Güler, E.; Uğur, G.; Uğur, Ş.; Güler, M. A theoretical study for the band gap energies of the most common silica polymorphs. *Chin. J. Phys.* **2020**, *65*, 472–480. [CrossRef]
55. Tea, E.; Huang, J.; Hin, C. First principles study of band line up at defective metal-oxide interface: Oxygen point defects at Al/SiO_2interface. *J. Phys. D Appl. Phys.* **2016**, *49*, 095304. [CrossRef]
56. Uzum, A.; Kanmaz, I. Passivation properties of HfO_2-SiO_2 mixed metal oxide thin films with low reflectivity on silicon substrates for semiconductor devices. *Thin Solid Films* **2021**, *738*, 138965. [CrossRef]
57. Okoshi, M.; Iyono, M.; Inoue, N.; Yamashita, T. Photochemical welding of silica microspheres to silicone rubber by ArF excimer laser. *Appl. Surf. Sci.* **2009**, *255*, 9796–9799. [CrossRef]
58. Jaehnike, F.; Pham, D.V.; Anselmann, R.; Bock, C.; Kunze, U. High-Quality Solution-Processed Silicon Oxide Gate Dielectric Applied on Indium Oxide Based Thin-Film Transistors. *ACS Appl. Mater. Interfaces* **2015**, *7*, 14011–14017. [CrossRef]

59. Bhatt, V.; Chandra, S. Silicon dioxide films by RF sputtering for microelectronic and MEMS applications. *J. Micromechanics Microengineering* **2007**, *17*, 1066–1077. [CrossRef]
60. Cross, R.B.M.; De Souza, M.M.; Deane, S.C.; Young, N.D. A Comparison of the Performance and Stability of ZnO-TFTs With Silicon Dioxide and Nitride as Gate Insulators. *IEEE Trans. Electron Devices* **2008**, *55*, 1109–1115. [CrossRef]
61. Ho, W.-J.; Lin, J.-C.; Liu, J.-J.; Bai, W.-B.; Shiao, H.-P. Electrical and Optical Characterization of Sputtered Silicon Dioxide, Indium Tin Oxide, and Silicon Dioxide/Indium Tin Oxide Antireflection Coating on Single-Junction GaAs Solar Cells. *Materials* **2017**, *10*, 700. [CrossRef]
62. Ashok, A.; Pal, P. Investigation of anodic silicon dioxide thin films for microelectromechanical systems applications. *Micro Nano Lett.* **2014**, *9*, 830–834. [CrossRef]
63. Ihlemann, J. Laser Based Rapid Fabrication of SiO_2-phase Masks for Efficient UV-laser Micromachining. *J. Laser Micro/Nanoengineering* **2009**, *4*, 100–103. [CrossRef]
64. Bailey, R.A.; Nevin, J.H. Thin-Film Multilayer Capacitors Using Pyrolytically Deposited Silicon Dioxide. *IEEE Trans. Parts Hybrids Packag.* **1976**, *12*, 361–364. [CrossRef]
65. Salawu, S.; Obalalu, A.; Fatunmbi, E.; Oderinu, R. Thermal Prandtl-Eyring hybridized MoS_2-SiO_2/$C_3H_8O_2$ and SiO_2-$C_3H_8O_2$ nanofluids for effective solar energy absorber and entropy optimization: A solar water pump implementation. *J. Mol. Liq.* **2022**, *361*, 119608. [CrossRef]
66. Talib, S.; Azmi, W.; Zakaria, I.; Mohamed, W.; Mamat, A.; Ismail, H.; Daud, W. Thermophysical Properties of Silicon Dioxide (SiO_2) in Ethylene Glycol/Water Mixture for Proton Exchange Membrane Fuel Cell Cooling Application. *Energy Procedia* **2015**, *79*, 366–371. [CrossRef]
67. Yao, Y.; Zhang, J.; Xue, L.; Huang, T.; Yu, A. Carbon-coated SiO_2 nanoparticles as anode material for lithium ion batteries. *J. Power Sources* **2011**, *196*, 10240–10243. [CrossRef]
68. Dong, X.; Zheng, X.; Deng, Y.; Wang, L.; Hong, H.; Ju, Z. SiO_2/N-doped graphene aerogel composite anode for lithium-ion batteries. *J. Mater. Sci.* **2020**, *55*, 13023–13035. [CrossRef]
69. Zhang, M.; Li, L.; Jian, X.; Zhang, S.; Shang, Y.; Xu, T.; Dai, S.; Xu, J.; Kong, D.; Wang, Y.; et al. Free-standing and flexible CNT/(Fe@Si@SiO_2) composite anodes with kernel-pulp-skin nanostructure for high-performance lithium-ion batteries. *J. Alloys Compd.* **2021**, *878*, 160396. [CrossRef]
70. Si, L.; Yan, K.; Li, C.; Huang, Y.; Pang, X.; Yang, X.; Sui, D.; Zhang, Y.; Wang, J.; Xu, C.C. Binder-free SiO_2 nanotubes/carbon nanofibers mat as superior anode for lithium-ion batteries. *Electrochimica Acta* **2022**, *404*, 139747. [CrossRef]
71. Afanas'Ev, V.V.; Stesmans, A.; Cherkaoui, K.; Hurley, P.K. Electron energy band alignment at the (100)Si/MgO interface. *Appl. Phys. Lett.* **2010**, *96*, 052103. [CrossRef]
72. Selvi, K.T.; Mangai, K.A.; Priya, M.; Sagadevan, S. Investigation of the dielectric and impedance properties of ZnO/MgO nanocomposite. *Phys. B Condens. Matter* **2020**, *594*, 412355. [CrossRef]
73. Huang, S.; Kang, B.; Duan, L.; Zhang, D. Highly efficient inverted polymer solar cells by using solution processed MgO/ZnO composite interfacial layers. *J. Colloid Interface Sci.* **2020**, *583*, 178–187. [CrossRef]
74. Farag, A.; Ashery, A.; Salem, M. Electrical, dielectric characterizations and optoelectronic applications of epitaxially grown Co/n-CuO/p-Si heterojunctions. *Superlattices Microstruct.* **2019**, *135*, 106277. [CrossRef]
75. Jiang, G.; Liu, A.; Liu, G.; Zhu, C.; Meng, Y.; Shin, B.; Fortunato, E.; Martins, R.; Shan, F. Solution-processed high-k magnesium oxide dielectrics for low-voltage oxide thin-film transistors. *Appl. Phys. Lett.* **2016**, *109*, 183508. [CrossRef]
76. Hornak, J.; Trnka, P.; Kadlec, P.; Michal, O.; Mentlík, V.; Šutta, P.; Csányi, G.M.; Tamus, Z. Magnesium Oxide Nanoparticles: Dielectric Properties, Surface Functionalization and Improvement of Epoxy-Based Composites Insulating Properties. *Nanomaterials* **2018**, *8*, 381. [CrossRef]
77. Subramanian, M.A.; Shannon, R.D.; Chai, B.H.T.; Abraham, M.M.; Wintersgill, M.C. Dielectric constants of BeO, MgO, and CaO using the two-terminal method. *Phys. Chem. Miner.* **1989**, *16*, 741–746. [CrossRef]
78. Lim, J.Y.; Oh, J.S.; Ko, B.; Cho, J.W.; Kang, S.O.; Cho, G.; Uhm, H.S.; Choi, E.H. Work function of MgO single crystals from ion-induced secondary electron emission coefficient. *J. Appl. Phys.* **2003**, *94*, 764–769. [CrossRef]
79. Lee, J.H.; Kim, H.S.; Kim, S.H.; Jang, N.W.; Yun, Y. Characterization of magnesium oxide gate insulators grown using RF sputtering for ZnO thin-film transistors. *Curr. Appl. Phys.* **2014**, *14*, 794–797. [CrossRef]
80. Arora, S. ZnO/MgO/ITO structured thin film transistor for ultraviolet photo detector application. *Mater. Today Proc.* **2020**, *30*, 150–152. [CrossRef]
81. Massarotti, D.; Bauch, T.; Lombardi, F.; Tafuri, F. Josephson and charging effect in mesoscopic superconducting devices. In *Superconductors at the Nanoscale*; De Gruyter: Berlin, Germany, 2017; pp. 309–338. [CrossRef]
82. Yeung, G.; Reich, C.; Onno, A.; Bothwell, A.; Danielson, A.; Holman, Z.; Sampath, W.S.; Wolden, C.A. Robust passivation of CdSeTe based solar cells using reactively sputtered magnesium zinc oxide. *Sol. Energy Mater. Sol. Cells* **2021**, *233*, 111388. [CrossRef]
83. Merachtsaki, D.; Tsardaka, E.-C.; Anastasiou, E.; Zouboulis, A. Anti-corrosion properties of magnesium oxide/magnesium hydroxide coatings for application on concrete surfaces (sewerage network pipes). *Constr. Build. Mater.* **2021**, *312*, 125441. [CrossRef]
84. Xu, K.; Lin, F.; Dou, X.; Zheng, M.; Tan, W.; Wang, C. Recovery of ammonium and phosphate from urine as value-added fertilizer using wood waste biochar loaded with magnesium oxides. *J. Clean. Prod.* **2018**, *187*, 205–214. [CrossRef]

85. Materials Data on Li_2O (SG:225) by Materials Project. 2014. Available online: https://materialsproject.org/materials/mp-1960 (accessed on 1 November 2022).
86. Ha, Y.; Schulze, M.C.; Frisco, S.; Trask, S.E.; Teeter, G.; Neale, N.R.; Veith, G.M.; Johnson, C.S. Li_2O-Based Cathode Additives Enabling Prelithiation of Si Anodes. *Appl. Sci.* **2021**, *11*, 12027. [CrossRef]
87. Dyer, C.; Moseley, P.; Ogumi, Z.; Rand, D.; Scrosati, B. *Encyclopedia of Electrochemical Power Sources*; Elsevier Science & Technology: Amsterdam, The Netherlands, 2009.
88. Donato, A. A critical review of Li_2O ceramic breeder material properties correlations and data. *Fusion Eng. Des.* **1998**, *38*, 369–392. [CrossRef]
89. Mosqueda, H.A.; Vazquez, C.; Bosch, P.; Pfeiffer, H. Chemical sorption of carbon dioxide (CO_2) on lithium oxide (Li_2O). *Chem. Mater.* **2006**, *18*, 2307–2310. [CrossRef]
90. Sun, Y.; Lee, H.-W.; Seh, Z.W.; Liu, N.; Sun, J.; Li, Y.; Cui, Y. High-capacity battery cathode prelithiation to offset initial lithium loss. *Nat. Energy* **2016**, *1*, 15008. [CrossRef]
91. Qiao, Y.; Yang, H.; Chang, Z.; Deng, H.; Li, X.; Zhou, H. A high-energy-density and long-life initial-anode-free lithium battery enabled by a Li_2O sacrificial agent. *Nat. Energy* **2021**, *6*, 653–662. [CrossRef]
92. Guo, R.; Gallant, B.M. Li_2O Solid Electrolyte Interphase: Probing Transport Properties at the Chemical Potential of Lithium. *Chem. Mater.* **2020**, *32*, 5525–5533. [CrossRef]
93. Lowe, J.S.; Siegel, D.J. Modeling the Interface between Lithium Metal and Its Native Oxide. *ACS Appl. Mater. Interfaces* **2020**, *12*, 46015–46026. [CrossRef]
94. Zheng, H.; Liu, Y.; Mao, S.X.; Wang, J.; Huang, J. Beam-assisted large elongation of in situ formed Li_2O nanowires. *Sci. Rep.* **2012**, *2*, 542. [CrossRef]
95. Attaa, T.S.; Abd, A.N.; Zoory, M.J. Fabrication of Al/Li_2O/PSi/ Si/Al heterojunction for photodetector and solar cell applications. *Mater. Today Proc.* **2021**, *49*, 3607–3614. [CrossRef]
96. Vijayalakshmi, L.; Kumar, K.N.; Kumar, G.B.; Hwang, P. Structural, dielectric and photoluminescence properties of Nd^{3+} doped Li_2O-LiF-B_2O_3-ZnO multifunctional optical glasses for solid state laser applications. *J. Non-Crystalline Solids* **2017**, *475*, 28–37. [CrossRef]
97. Al Hussan, S.M.A.; Bakr, N.A.; Abd, A.N. Improve the Performance of Porous Silicon for solar application by the embedding of Lithium Oxide nanoparticle. *IOP Conf. Ser. Mater. Sci. Eng.* **2020**, *928*. [CrossRef]
98. Yang, W.; Kim, D.Y.; Yang, L.; Li, N.; Tang, L.; Amine, K.; Mao, H. Oxygen-Rich Lithium Oxide Phases Formed at High Pressure for Potential Lithium–Air Battery Electrode. *Adv. Sci.* **2017**, *4*, 1600453. [CrossRef]
99. Al-Ubaidi, M.R.; Anno, J.N. The Production of Lithium Oxide Microspheres from the Disintegration of a Liquid Jet. *Fusion Technol.* **1989**, *16*, 464–468. [CrossRef]
100. Abo-Mosallam, H.; Ibrahim, S.; Mahdy, E.A. New high nickel-containing glass-ceramics based on Li_2O–CaO–SiO_2 eutectic (954 °C) system for magnetic applications. *J. Non-Crystalline Solids* **2022**, *580*, 121385. [CrossRef]
101. Jamil, S.M.; Othman, M.H.D.; Rahman, M.A.; Jaafar, J.; Ismail, A.F.; Mohamed, M.A. Role of lithium oxide as a sintering aid for a CGO electrolyte fabricated via a phase inversion technique. *RSC Adv.* **2015**, *5*, 58154–58162. [CrossRef]
102. Edström, K.; Herstedt, M.; Abraham, D.P. A new look at the solid electrolyte interphase on graphite anodes in Li-ion batteries. *J. Power Sources* **2006**, *153*, 380–384. [CrossRef]
103. Aurbach, D.; Dekker, M. *Nonaqueous Electrochemistry*; CRC Press: Boca Raton, FL, USA, 1999.
104. Peled, E.; Menkin, S. Review—SEI: Past, Present and Future. *J. Electrochem. Soc.* **2017**, *164*, A1703–A1719. [CrossRef]
105. Peled, E.; Golodnitsky, D.; Penciner, J. The Anode/Electrolyte Interface. In *Handbook of Battery Materials*; Wiley-VCH: Weinheim, Germany, 1998; pp. 419–456. [CrossRef]
106. Goodenough, J.B.; Hong, H.Y.-P.; Kafalas, J.A. Fast Na^+-ion transport in skeleton structures. *Mater. Res. Bull.* **1976**, *11*, 203–220. [CrossRef]
107. Roy, S.; Kumar, P.P. Influence of Cationic ordering on ion transport in NASICONs: Molecular dynamics study. *Solid State Ionics* **2013**, *253*, 217–222. [CrossRef]
108. Guin, M.; Tietz, F. Survey of the transport properties of sodium superionic conductor materials for use in sodium batteries. *J. Power Sources* **2015**, *273*, 1056–1064. [CrossRef]
109. Susman, S.; Delbecq, C.; Brun, T.; Prince, E. Fast ion transport in the NASICON analog $Na_3Sc_2(PO_4)_3$: Structure and conductivity. *Solid State Ionics* **1983**, *9–10*, 839–844. [CrossRef]
110. Hong, H.Y.-P. Crystal structures and crystal chemistry in the system $Na_{1+x}Zr_2Si_xP_{3-x}O_{12}$. *Mater. Res. Bull.* **1976**, *11*, 173–182. [CrossRef]
111. Jiang, T.; Wei, Y.; Pan, W.; Li, Z.; Ming, X.; Chen, G.; Wang, C. Preparation and electrochemical studies of $Li_3V_2(PO_4)_3$/Cu composite cathode material for lithium ion batteries. *J. Alloys Compd.* **2009**, *488*, L26–L29. [CrossRef]
112. Feng, J.; Lu, L.; Lai, M. Lithium storage capability of lithium ion conductor $Li_{1.5}Al_{0.5}Ge_{1.5}(PO_4)_3$. *J. Alloys Compd.* **2010**, *501*, 255–258. [CrossRef]
113. Yang, K.-Y.; Wang, J.-W.; Fung, K.-Z. Roles of lithium ions and La/Li-site vacancies in sinterability and total ionic conduction properties of polycrystalline $Li_3xLa_2/_3-xTiO_3$ solid electrolytes ($0.21 \leq 3x \leq 0.50$). *J. Alloys Compd.* **2008**, *458*, 415–424. [CrossRef]
114. Feng, J.; Xia, H.; Lai, M.O.; Lu, L. NASICON-structured $LiGe_2(PO_4)_3$ with improved cyclability for high-performance lithium batteries. *J. Phys. Chem. C* **2009**, *113*, 20514–22052. [CrossRef]

115. Govindaraj, G. Synthesis, characterization and ion dynamic studies of NASICON type glasses. *Solid State Ionics* **2002**, *147*, 49–59. [CrossRef]
116. Zhang, Q.; Wen, Z.; Liu, Y.; Song, S.; Wu, X. Na+ ion conductors of glass–ceramics in the system Na_1+xAlxGe$_2$−xP$_3$O$_{12}$(0.3 ≤ x ≤ 1.0). *J. Alloys Compd.* **2009**, *479*, 494–499. [CrossRef]
117. Anantharamulu, N.; Rao, K.K.; Vithal, M.; Prasad, G. Preparation, characterization, impedance and thermal expansion studies of $Mn_{0.5}MSb(PO_4)_3$ (M = Al, Fe and Cr). *J. Alloys Compd.* **2009**, *479*, 684–691. [CrossRef]
118. Fu, J. Superionic conductivity of glass-ceramics in the system Li_2O-Al_2O_3-TiO_2-P_2O_5. *Solid State Ionics* **1997**, *96*, 195–200. [CrossRef]
119. Li, X.; Qu, M.; Yu, Z. Structural and electrochemical performances of Li_4Ti_{5-}xZrxO$_{12}$ as anode material for lithium-ion batteries. *J. Alloys Compd.* **2009**, *487*, L12–L17. [CrossRef]
120. Liu, S.-Q.; Li, S.-C.; Huang, K.-L.; Gong, B.-L.; Zhang, G. Kinetic study on $Li_{2.8}(V_{0.9}Ge_{0.1})2(PO_4)_3$ by EIS measurement. *J. Alloys Compd.* **2008**, *450*, 499–504. [CrossRef]
121. Yao, X.; Xie, S.; Nian, H.; Chen, C. Spinel $Li_4Ti_5O_{12}$ as a reversible anode material down to 0 V. *J. Alloys Compd.* **2008**, *465*, 375–379. [CrossRef]
122. Zhang, C.; Tu, J.; Huang, X.; Yuan, Y.; Wang, S.; Mao, F. Preparation and electrochemical performances of nanoscale FeSn2 as anode material for lithium ion batteries. *J. Alloys Compd.* **2008**, *457*, 81–85. [CrossRef]
123. Arbi, K.; Rojo, J.M.; Sanz, J. Lithium mobility in titanium based Nasicon $Li_{1+x}Ti_{2-x}Al_x(PO_4)_3$ and $LiTi_{2-x}$ $Zr_x(PO_4)_3$ materials followed by NMR and impedance spectroscopy. *J. Eur. Ceram. Soc.* **2007**, *27*, 4215–4218. [CrossRef]
124. Peña, J.S.; Sandu, I.; Joubert, O.; Pascual, F.S.; Areán, C.O.; Brousse, T. Electrochemical reaction between lithium and β-quartz GeO_2. *Electrochem. Solid-State Lett.* **2004**, *7*, A278. [CrossRef]
125. Lee, H.; Kim, M.G.; Choi, C.H.; Sun, Y.K.; Yoon, C.S.; Cho, J. Surface-stabilized amorphous germanium nanoparticles for lithium-storage material. *J. Phys. Chem. B* **2005**, *109*, 20719–20723. [CrossRef]
126. DeWees, R.; Wang, H. Synthesis and Properties of NaSICON-type LATP and LAGP Solid Electrolytes. *ChemSusChem* **2019**, *12*, 3713–3725. [CrossRef]
127. Kazakevičius, E.; Šalkus, T.; Dindune, A.; Kanepe, Z.; Ronis, J.; Kežionis, A.; Kazlauskienė, V.; Miškinis, J.; Selskienė, A.; Selskis, A. La-doped $LiTi_2(PO_4)_3$ ceramics. *Solid State Ionics* **2008**, *179*, 51–56. [CrossRef]
128. Rohde, M.; Cui, Y.; Ziebert, C.; Seifert, H.J. Thermophysical Properties of Lithium Aluminum Germanium Phosphate with Different Compositions. *Int. J. Thermophys.* **2020**, *41*, 31. [CrossRef]
129. Schroeder, M.; Glatthaar, S.; Binder, J.R. Influence of spray granulation on the properties of wet chemically synthesized $Li_{1.3}Ti_{1.7}Al_{0.3}(PO_4)_3$ (LATP) powders. *Solid State Ionics* **2011**, *201*, 49–53. [CrossRef]
130. Fergus, J.W. Ceramic and polymeric solid electrolytes for lithium-ion batteries. *J. Power Sources* **2010**, *195*, 4554–4569. [CrossRef]
131. Francisco, B.E.; Stoldt, C.R.; M'Peko, J.-C. Lithium-Ion Trapping from Local Structural Distortions in Sodium Super Ionic Conductor (NASICON) Electrolytes. *Chem. Mater.* **2014**, *26*, 4741–4749. [CrossRef]
132. Cretin, M.; Fabry, P. Comparative study of lithium ion conductors in the system $Li_{1+x}Al_xA_2-xIV$ $(PO_4)_3$ with AIV = Ti or Ge and 0 ≤ x ≤ 0·7 for use as Li+ sensitive membranes. *J. Eur. Ceram. Soc.* **1999**, *19*, 2931–2940. [CrossRef]
133. Dumon, A.; Huang, M.; Shen, Y.; Nan, C.W. High Li ion conductivity in strontium doped $Li_7La_3Zr_2O_{12}$ garnet. *Solid State Ionics* **2013**, *243*, 36–41. [CrossRef]
134. He, K.; Zu, C.; Wang, Y.; Han, B.; Yin, X.; Zhao, H.; Liu, Y.; Chen, J. Stability of lithium ion conductor NASICON structure glass ceramic in acid and alkaline aqueous solution. *Solid State Ionics* **2013**, *254*, 78–81. [CrossRef]
135. Chowdari, B. XPS and ionic conductivity studies on Li_2O–Al_2O_3–(TiO_2 or GeO_2)–P2O5 glass–ceramics. *Solid State Ionics* **2000**, *136–137*, 1067–1075. [CrossRef]
136. Aboulaich, A.; Bouchet, R.; Delaizir, G.; Seznec, V.; Tortet, L.; Morcrette, M.; Rozier, P.; Tarascon, J.-M.; Viallet, V.; Dollé, M. A New Approach to Develop Safe All-Inorganic Monolithic Li-Ion Batteries. *Adv. Energy Mater.* **2011**, *1*, 179–183. [CrossRef]
137. Arbi, K.; Bucheli, W.; Jiménez, R.; Sanz, J. High lithium ion conducting solid electrolytes based on NASICON $Li_{1+x}Al_xM_{2-x}(PO_4)_3$ materials (M = Ti, Ge and 0 ≤ x ≤ 0.5). *J. Eur. Ceram. Soc.* **2015**, *35*, 1477–1484. [CrossRef]
138. Shi, J.; Xia, Y.; Han, S.; Fang, L.; Pan, M.; Xu, X.; Liu, Z. Lithium ion conductive $Li_{1.5}Al_{0.5}Ge_{1.5}(PO_4)_3$ based inorganic–organic composite separator with enhanced thermal stability and excellent electrochemical performances in 5 V lithium ion batteries. *J. Power Sources* **2015**, *273*, 389–395. [CrossRef]
139. Liu, Y.; Li, C.; Li, B.; Song, H.; Cheng, Z.; Chen, M.; He, P.; Zhou, H. Germanium Thin Film Protected Lithium Aluminum Germanium Phosphate for Solid-State Li Batteries. *Adv. Energy Mater.* **2018**, *8*, 1702374. [CrossRef]
140. Vernoux, P.; Gaillard, F.; Lopez, C.; Siebert, E. Coupling catalysis to electrochemistry: A solution to selective reduction of nitrogen oxides in lean-burn engine exhausts? *J. Catal.* **2003**, *217*, 203–208. [CrossRef]
141. Roy, R.; Vance, E.; Alamo, J. [NZP], a new radiophase for ceramic nuclear waste forms. *Mater. Res. Bull.* **1982**, *17*, 585–589. [CrossRef]
142. Nakayama, S.; Itoh, K. Immobilization Technique of Cesium to $HZr_2(PO_4)_3$Using an Autoclave. *J. Nucl. Sci. Technol.* **2003**, *40*, 631–633. [CrossRef]
143. Scheetz, B.; Agrawal, D.; Breval, E.; Roy, R. Sodium zirconium phosphate (NZP) as a host structure for nuclear waste immobilization: A review. *Waste Manag.* **1994**, *14*, 489–505. [CrossRef]

144. Li, B.; Qing, Z.; Li, Y.; Li, H.; Zhang, S. Effect of CaO content on structure and properties of low temperature co-fired glass–ceramic in the Li_2O–Al_2O_3–SiO_2 system. *J. Mater. Sci. Mater. Electron.* **2016**, *27*, 2455–2459. [CrossRef]
145. Li, B.; Duan, D.; Long, Q. Effects of TiO_2 on microstructures and properties of Li_2O–Al_2O_3–SiO_2 glass–ceramics for LTCC substrates. *J. Mater. Sci. Mater. Electron.* **2016**, *27*, 7240–7245. [CrossRef]
146. Soares, V.O.; Peitl, O.; Zanotto, E.D. New Sintered Li_2 O-Al_2 O_3 -SiO_2 Ultra-Low Expansion Glass-Ceramic. *J. Am. Ceram. Soc.* **2013**, *96*, 1143–1149. [CrossRef]
147. Chen, M.; He, F.; Shi, J.; Xie, J.; Yang, H.; Wan, P. Low Li_2O content study in Li_2O-Al_2O_3-SiO_2 glass-ceramics. *J. Eur. Ceram. Soc.* **2019**, *39*, 4988–4995. [CrossRef]
148. Braga, M.H.; Grundish, N.S.; Murchison, A.J.; Goodenough, J.B. Alternative strategy for a safe rechargeable battery. *Energy Environ. Sci.* **2016**, *10*, 331–336. [CrossRef]
149. Danzi, F.; Salgado, R.; Oliveira, J.; Arteiro, A.; Camanho, P.; Braga, M. Structural Batteries: A Review. *Molecules* **2021**, *26*, 2203. [CrossRef] [PubMed]
150. Xia, W.; Zhao, Y.; Zhao, F.; Adair, K.; Zhao, R.; Li, S.; Zou, R.; Zhao, Y.; Sun, X. Antiperovskite Electrolytes for Solid-State Batteries. *Chem. Rev.* **2022**, *122*, 3763–3819. [CrossRef] [PubMed]